ACSNANO Cite This: ACS Nano 2019, 13, 4049−4063 www.acsnano.org

ARTICLE

Targeting the Oncogene KRAS Mutant Pancreatic Cancer by Synergistic Blocking of Lysosomal Acidification and Rapid Drug Release

Chao Kong,[†] Yang Li,[‡] Zhengsheng Liu,[†] Junxiao Ye,[†] Zhaohui Wang,[‡] Ling Zhang,[†] Weijian Kong,[†] Huiqin Liu,[†] Chun Liu,[†] Huanhuan Pang,[§] Zeping Hu,[§] Jinming Gao,*[,‡] and Feng Qian*[,†]

[†]School of Pharmaceutical Sciences, Beijing Advanced Innovation Center for Structural Biology, and Key Laboratory of Bioorganic Phosphorus Chemistry & Chemical Biology (Ministry of Education), Tsinghua University, Beijing 100084, People's Republic of China

[‡]Department of Pharmacology, Simmons Comprehensive Cancer Center, University of Texas Southwestern Medical Center, Dallas, Texas 75390, United States

[§]School of Pharmaceutical Sciences, Tsinghua University, Beijing 100084, People's Republic of China

Supporting Information

ABSTRACT: **Survival of KRAS mutant pancreatic cancer is critically dependent on reprogrammed metabolism including elevated macropinocytosis, autophagy, and lysosomal degradation of proteins. Lysosomal acidification is indispensable to protein catabolism, which makes it an exploitable metabolic target for KRAS mutant pancreatic cancer. Herein we investigated ultra-pH-sensitive micelles (UPSM) with pH-specific buffering of organelle pH and rapid drug release as a promising therapy against pancreatic cancer. UPSM undergo micelle−unimer phase transition at their apparent pK_a, with dramatically increased buffer capacity in a narrow pH range (<0.3 pH). Cell studies including amino acid profiling showed that UPSM inhibited lysosomal catabolism more efficiently than conventional lysosomotropic agents (*e.g.*, chloroquine) and induced cell apoptosis under starved condition. Moreover, pH-triggered rapid drug release from triptolide prodrug-loaded UPSM (T-UPSM) significantly enhanced cytotoxicity over non-pH-sensitive micelles (T-NPSM). Importantly, T-UPSM demonstrated superior safety and antitumor efficacy over triptolide and T-NPSM in KRAS mutant pancreatic cancer mouse models. Our findings suggest that the ultra-pH-sensitive nanoparticles are a promising therapeutic platform to treat KRAS mutant pancreatic cancer through simultaneous lysosomal pH buffering and rapid drug release.**

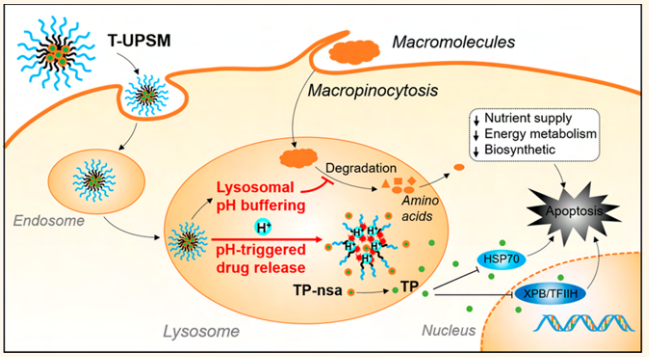

KEYWORDS: *mutant KRAS, pancreatic cancer, lysosomal buffering, ultra-pH-sensitive micelles, drug delivery*

Pancreatic cancer is becoming the most intractable disease globally. The majority (85−90%) of pancreatic cancers are pancreatic ductal adenocarcinoma (PDAC) with a 5-year survival rate less than 6%.[1−4] Multiple factors contribute to the grim prognosis of PDAC: (1) Almost 95% of PDAC are transformed by oncogenic KRAS that is considered "undruggable" until recently;[5−7] (2) the complex tumor microenvironment not only promotes tumor progression but also prevents drug delivery;[8,9] (3) an immunosuppressive tumor stroma that leads to the failure of immune check-point inhibitors in recent PDAC clinical trials, despite their revolutionary success in other cancer types.[9,10] The absence of successful targets and effective therapeutic drugs raises the urgency of other potential therapeutic approaches against PDAC.[2,11,12]

PDAC are poorly vascularized and nutrient-stressed.[8,13,14] Oncogenic KRAS drives reprogrammed metabolism, including elevated macropinocytosis[3,5,13,15] and autophagy,[3,5,16] to scavenge extracellular and intracellular nutrients for cell growth and survival.[2,6,16,17] The survival of PDAC was found to be critically dependent on these reprogrammed metabolic

Received: October 29, 2018
Accepted: March 26, 2019
Published: March 26, 2019

DOI: 10.1021/acsnano.8b08246
ACS Nano 2019, 13, 4049−4063

processes. Targeting the abnormal "metabolic bottlenecks"[18] has become an increasingly attractive strategy for treating KRAS mutant pancreatic cancer.[5,6,14,18−20]

Lysosomes, as the central organelle for catabolism of extracellular and intracellular components,[21] mediate a range of biological processes including cellular clearance and secretion, nutrient sensing, and metabolism.[22,23] KRAS mutation has been investigated to increase lysosomal acidification and activity by the pH barcode sensors (hybrid ultra-pH-sensitive nanoprobes)[24] and the commercial pH-sensitive dye Oregon Green 514,[16] and macromolecules in macropinosomes or autophagosomes are eventually transported to lysosomes/autolysosomes and degraded by acid-sensitive hydrolases to produce metabolic intermediates, including amino acids, for nutrient supply and vital biosynthetic reactions.[13,18,21−23,25−29] Lysosomal acidification is indispensable to lysosomal catabolism by maintaining optimal activity of acid hydrolases[26,30] and is vital to regulate the efflux of lysosomal amino acids.[27] Therefore, inhibition of lysosomal acidification to disrupt lysosomal catabolism can serve as a promising therapeutic strategy against KRAS mutant PDAC.

In this study, we report ultra-pH-sensitive micelles (UPSM), with 30−300-fold stronger pH buffer capacity than commonly used lysosomotropic agents such as chloroquine (CQ),[31] to simultaneously inhibit lysosomal acidification and enhance therapeutic delivery. We observed that UPSM alone inhibited lysosomal catabolism, reduced KRAS mutant PDAC cell viability under starved condition, and inhibited tumor progression in PDAC mouse models. In contrast, non-pH-sensitive micelles (NPSM) had no obvious effect either *in vitro* or *in vivo*. Additionally, acidic organelle pH triggers a rapid dissociation of UPSM at pH 6 to release triptolide-naphthalene sulfonamide (TP-nsa). Esterase-catalyzed conversion of TP-nsa to the parent drug triptolide (TP) resulted in cell apoptosis by inhibiting HSP70 expression and by covalently binding to human xeroderma pigmentosum B (XPB).[32,33] TP-nsa-loaded UPSM (T-UPSM) enhanced the cytotoxicity compared with T-NPSM and showed synergistic inhibition of tumor growth and metastasis by the nanoparticle carriers as well as encapsulated drugs, as illustrated in Scheme 1, and significantly prolonged the animal survival in the KRAS mutant PDAC mouse model.

RESULTS

Preparation and Characterization of T-UPSM. Poly(ethylene glycol)-*block*-poly(dipropylaminoethyl methacrylate) block copolymer (PEG-*b*-PDPA, the PEG and PDPA segments were 5 and 16.6 kDa, respectively) was used to prepare UPSM.[34] Poly(ethylene glycol)-*block*-poly(D,L-lactic acid) (PEG-*b*-PLA) block copolymer (10 kDa, the PEG and PLA segments were 5 kDa) was used to prepare the non-pH-sensitive micelles, NPSM. In our preliminary study we found that the encapsulation efficacy of TP in NPSM or UPSM was less than 20%, and the stability of TP-loaded micelles was another problem due to the hydrophilicity (the LogP of TP is 0.69) and high crystallization tendency of TP.[35−37] To achieve efficient drug encapsulation and to improve the stability of micelles, we synthesized a hydrophobic prodrug of triptolide, TP-nsa (Figure 1a and Figures S1−S4), with a calculated LogP of 2.33 ± 0.85. TP-nsa can be readily converted into the parent drug triptolide in the presence of esterase with ∼80% conversion after 6 h of incubation with 20 U/mL of porcine liver esterase (PLE) (Figure S5). Cell viability assays revealed

Scheme 1. Schematic of targeting KRAS-mutant pancreatic cancer by lysosomal pH buffering and drug release using ultra-pH-sensitive micelles (UPSM). Oncogenic KRAS mutation elevates macropinocytosis and lysosomal metabolism. Blocking lysosomal acidification with T-UPSM disrupts lysosomal degradation of macromolecules and hinders nutrient supply for survival. Moreover, pH-triggered drug release and conversion of triptolide-naphthalene sulfonamide (TP-nsa) led to cell apoptosis and synergistic therapeutic outcomes

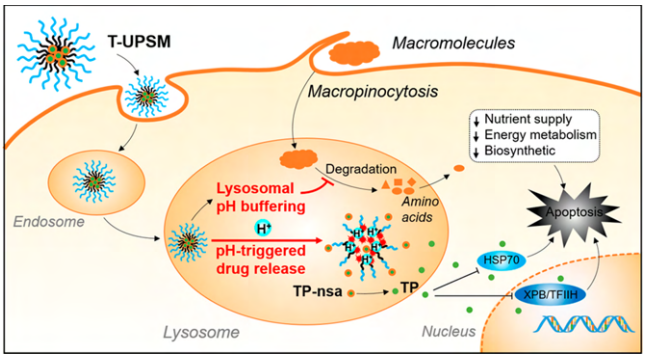

that neither nsa nor TP-nsa (without PLE) was cytotoxic to pancreatic cancer cells (Figure S6).

T-UPSM and T-NPSM were prepared by inverse solvation[31] and solvent-evaporation methods,[38] respectively (Figure 1b,c). The major physicochemical properties of T-UPSM and T-NPSM are shown in Table 1. T-UPSM had similar nanoparticle size and distribution to T-NPSM, and both micelles had negative zeta-potential. The critical micelle concentrations (CMC) for UPSM and NPSM were ∼1.5 and 1 μg/mL, respectively (Figure 1d,e and Figure S7). Both micelles displayed spherical morphology and had similar narrow size distributions with average diameters of 34−37 nm (Figure 1d,e and Table 1). The physicochemical characteristics of polymer nanoparticles determined the cellular uptake, transport, and circulation;[39−41] therefore the *in vivo* biodistribution of T-NPSM and T-UPSM would be very similar as well.

pH Buffering Effect of T-UPSM. We first examined the pH buffering effect of blank micelles using a modified pH titration method.[34,42] Briefly, HCl (0.1 M) was added incrementally to titrate both micelles (1 mg/mL polymer) in saline. UPSM displayed notable pH plateaus at pH 6.0, as previously observed,[31] whereas the pH of NPSM decreased proportionally with the addition of HCl (Figure 2a), indicating that UPSM, but not NPSM, has a strong pH buffering effect. Since micellization of UPSM is critical for the pH buffering effect,[34,43] and the encapsulated hydrophobic drug may influence the self-assembly and dissociation of micelles,[44] we further evaluated the impact of drug encapsulation on the pH buffering effect of these micelles. The pH titration results confirmed that drug encapsulation had a minimal impact on the pH buffering capabilities: T-NPSM had no obvious pH buffering effect (Figure 2b), whereas T-UPSM (polymer concentration 1 mg/mL) showed the same pH plateaus at pH 6.0 (Figure 2a,c).

We further investigated the correlation between polymer concentration (1000, 500, 100, and 1 μg/mL) and pH buffering effect and capacity. The pH titration results demonstrated that the pH buffering effect of T-UPSM was

DOI: 10.1021/acsnano.8b08246
ACS Nano 2019, 13, 4049−4063

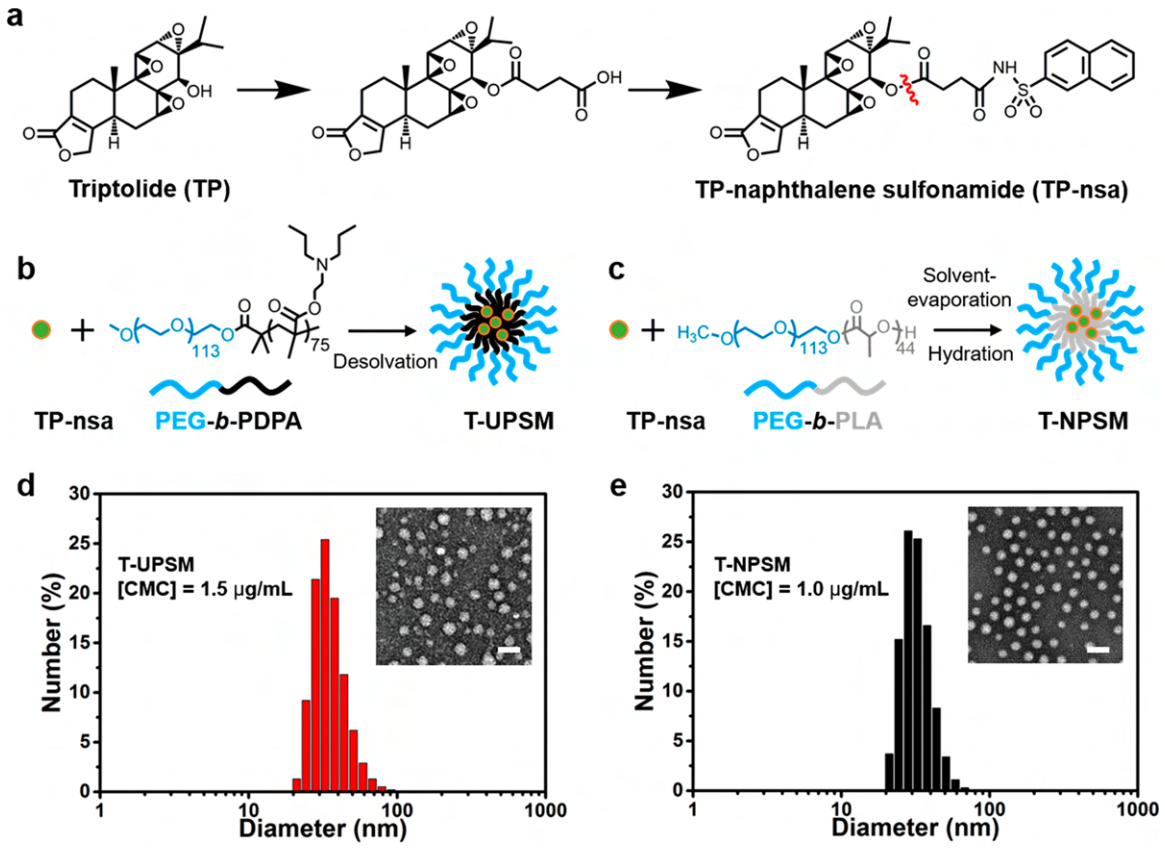

Figure 1. Preparation and characterization of T-UPSM and T-NPSM. (a) Synthesis of TP-naphthalene sulfonamide (TP-nsa) from triptolide (TP). Ester bond (indicated by the red wave line) is biodegradable by esterase. Preparation of (b) T-UPSM by solvent inversion method and (c) T-NPSM by solvent-evaporation method. Size distributions, CMC, and TEM images of (d) T-UPSM and (e) T-NPSM. Scale bar in TEM images: 50 nm.

Table 1. Physical Characterization of T-NPSM and T-UPSM

group	size[a] (nm)	PDI[b]	zeta-p (mV)	TDL[c] (%)	DL[d] (%)	EE[e] (%)
T-NPSM	34.4 ± 1.4	0.106 ± 0.005	−5.5 ± 1.6	5.12	5.10 ± 0.09	99.5 ± 1.7
T-UPSM	37.6 ± 1.9	0.115 ± 0.008	−1.0 ± 0.3	5.12	4.24 ± 0.15	82.0 ± 3.5

[a]Mean diameter measured by dynamic light scattering (DSL). [b]PDI, polydispersity index. [c]TDL, theoretical drug loading. [d]DL, drug loading. [e]EE, encapsulation efficiency.

concentration-dependent (Figure 2c). The pH buffering capacity is a quantitative measurement of the resistance of a buffer solution to pH change on addition of H^+.[31] The pH buffering capacity β calculated from the pH titration curves (Figure 2c) disclosed that T-UPSM specifically buffered the pH at 6.0, which is independent of the micelle concentration as long as it is above the CMC of the T-UPSM, *i.e.*, 1.5 μg/mL (Figure 2d). A linear correlation was found between the maximal buffering capacity β and polymer concentration of T-UPSM (Figure 2e).

To quantify the relationship between pH buffering effect and protonation degree of micelles, the pH change was plotted against the degree of protonation of tertiary amines in PEG-*b*-PDPA. Indeed, T-UPSM (100, 500, and 1000 μg/mL) could buffer solutions at pH ~6 until the protonation degree of micelles reached 90% (Figure 2f). The absence of pH buffering of the 1 μg/mL T-UPSM was likely due to its ultralow polymer concentration. In short, T-UPSM showed a strong and specific pH buffering effect at pH 6 when polymer concentration was above CMC, whereas no pH buffering effect was observed for T-NPSM. The pH buffering effect will not be altered in biological solutions, as confirmed by the pH titration in 100 μg/mL BSA and 10% (v/v) fetal bovine serum (FBS) solutions (Figure S8).

***In Vitro* pH-Responsive Behavior and Drug Release Profile of T-NPSM and T-UPSM.** As mentioned earlier, KRAS mutant PDAC cells display elevated macropinocytosis and lysosomal activity, and extracellular substances engulfed by macropinosomes or endosomes are eventually transported to lysosomes for degradation. To mimic the acidic lysosomal environment, we first assessed the pH-responsive behavior of T-UPSM *in vitro* by monitoring its change in particle size when pH is varied. The critical pH value leading to the dissociation of T-UPSM ranged from pH 5.75 to 6.0, with no particles existing below this pH (Figure 3a). This sharp change in particle size within ~0.25 pH units confirmed the ultra-pH sensitivity of T-UPSM. This pH sensitivity will not be altered in biological solutions, as shown in Figure S8. The critical pH value of 6.0 could ensure rapid dissociation of T-UPSM in late endosomes or lysosomes when the pH is as low as 4.5−5.5.[45,46] The morphology of T-UPSM upon pH titration further confirmed the pH-responsive behavior, where only random

DOI: 10.1021/acsnano.8b08246
ACS Nano 2019, 13, 4049−4063

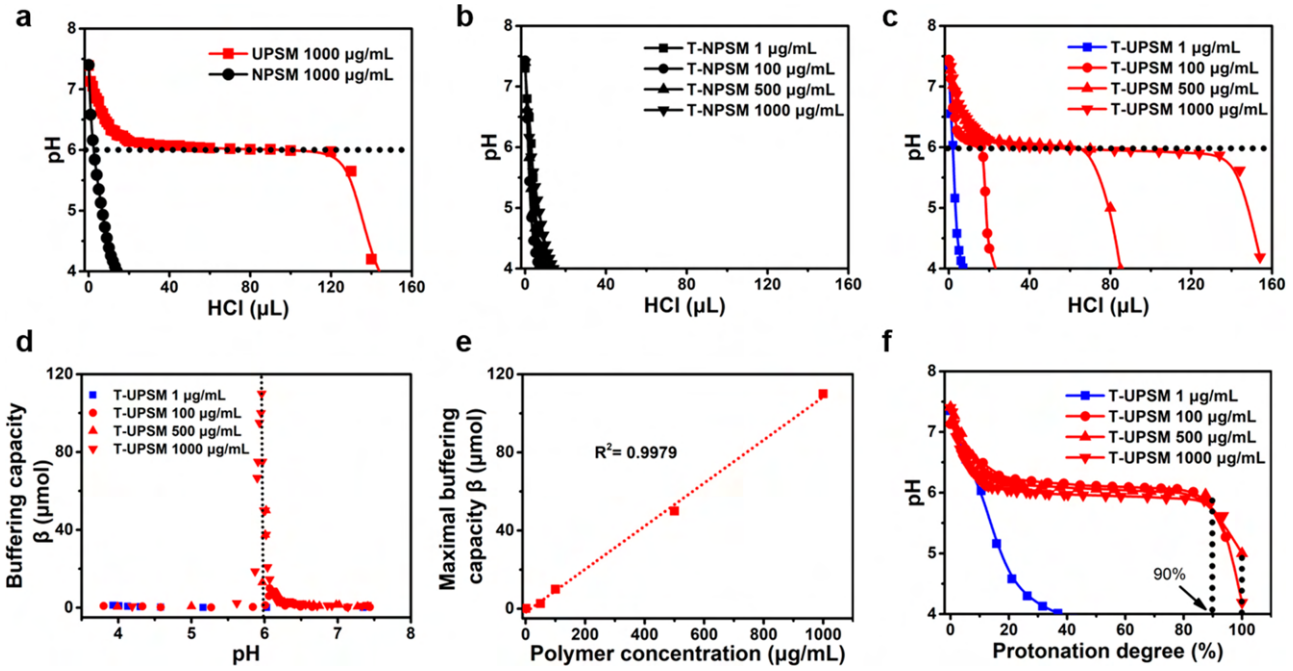

Figure 2. pH buffering effect of T-UPSM and T-NPSM. Change in the pH with HCl (0.1 M) titration of (a) UPSM (1000 μg/mL) and NPSM (1000 μg/mL), (b) T-NPSM (1, 100, 500, and 1000 μg/mL), and (c) T-UPSM (1, 100, 500, and 1000 μg/mL) in saline at room temperature. The dotted horizontal line in (a) and (c) indicates the pH plateau at pH 6. (d) Buffering capacity β (μmol/pH) of various polymer concentrations of T-UPSM plotted as a function of pH. The pH buffering capacity $\beta = -\frac{dn_{H^+}}{dpH}$, where dn_{H^+} is the quantity of added H^+ and dpH is the corresponding pH change. The dotted vertical line indicates the maximal buffering capacity at pH 6. (e) Maximal buffering capacity β as a function of various polymer concentrations of T-UPSM. The *R*-squared value is calculated by linear fitting. (f) pH change of T-UPSM solution plotted as a function of protonation degree. The two dotted vertical lines in (f) indicate 90% and 100% protonation, respectively.

polymer dispersions were observed at pH 5.5 instead of spherical nanoparticles (Figure 3c, upper panel).

We also evaluated the correlation between micellization and pH buffering effect by simultaneously monitoring the particle size and solution pH against the protonation of micelles. The apparent pK_a of T-UPSM was ~6, as shown in Figure 3b (apparent pK_a is defined as the pH where 50% of ionizable groups are protonated[34]). The critical micelle protonation degree (CMPD) indicates the threshold protonation degree of an individual polymer chain below which unimers self-assemble into micelles.[34] Dissociation of drug-loaded micelles occurred simultaneously with the loss of pH buffering effect, both at 90% of protonation degree, illustrating that both processes are co-dependent on micellization (Figure 3b). A schematic model for the proposed self-assembly, protonation, and pH-triggered dissociation of T-UPSM is shown in Figure 3c (lower panel).

We further compared the drug release profiles of T-NPSM and T-UPSM either under the physiological pH of 7.4 in blood or under an acidic lysosomal pH of 5.0. The drug release kinetics from T-NPSM remained fairly slow and essentially the same under either pH (Figure 3d). However, TP-nsa release from T-UPSM was much faster at pH 5.0 than at pH 7.4 (Figure 3e), presumably due to the immediate dissociation of T-UPSM at pH below its apparent pK_a (Figure 3b,c). These findings suggested that the T-UPSM could accelerate drug release in the late endosome or lysosome environments, which was confirmed in the following cell culture study.

UPSM Inhibit Lysosomal Catabolism More Efficiently than Lysosomotropic Agents. Before testing the pH buffering effect of UPSM on lysosomal acidification and catabolism, we first evaluated the extent of macropinocytosis by KRAS mutant PANC-1 cells. Macropinocytosis was identified to be the critical endocytosis mechanism for KRAS mutant cancer to nonspecifically take up extracellular proteins, lipids, and nanoparticles.[13,15,17,18] The PDAC tumor microenvironment is poorly vascularized and highly nutrient-deprived;[13,14] we thus assessed macropinocytosis of PANC-1 cells under both fed (complete medium with 10% FBS) and starved (Dulbecco's modified Eagle's medium (DMEM), FBS-free) cell culture conditions, using FITC-dextran as a marker of macropinocytosis.[47] Interestingly, FITC-dextran uptake by PANC-1 cells under starved condition was found to be 14-fold higher than that under fed condition (Figure 4a,b), suggesting the cells need to internalize extracellular nutrients to sustain their growth and survival under nutrient-deprived condition. The result was also consistent with the *in vivo* observation of KRAS mutant PDAC, which heavily relies on elevated macropinocytosis to scavenge extracellular nutrients such as serum albumins.[13,15,18] We also used EIPA, a widely used macropinocytosis inhibitor,[15,48] to inhibit the macropinocytosis of FITC-dextran by PANC-1 cells. The results showed that FITC-dextran uptake by PANC-1 cells was significantly reduced (Figure 4a,b). Moreover, the inhibition of macropinocytosis of PANC-1 cells by EIPA was concentration-dependent (Figure 4a,b), consistent with a previous report.[15]

We used dye-quenched bovine serum albumin (DQ-BSA), a self-quenched albumin that emits fluorescent signal upon protein degradation,[49] to evaluate the impact of pH buffering by UPSM on lysosomal catabolism. It was observed that little

DOI: 10.1021/acsnano.8b08246
ACS Nano 2019, 13, 4049−4063

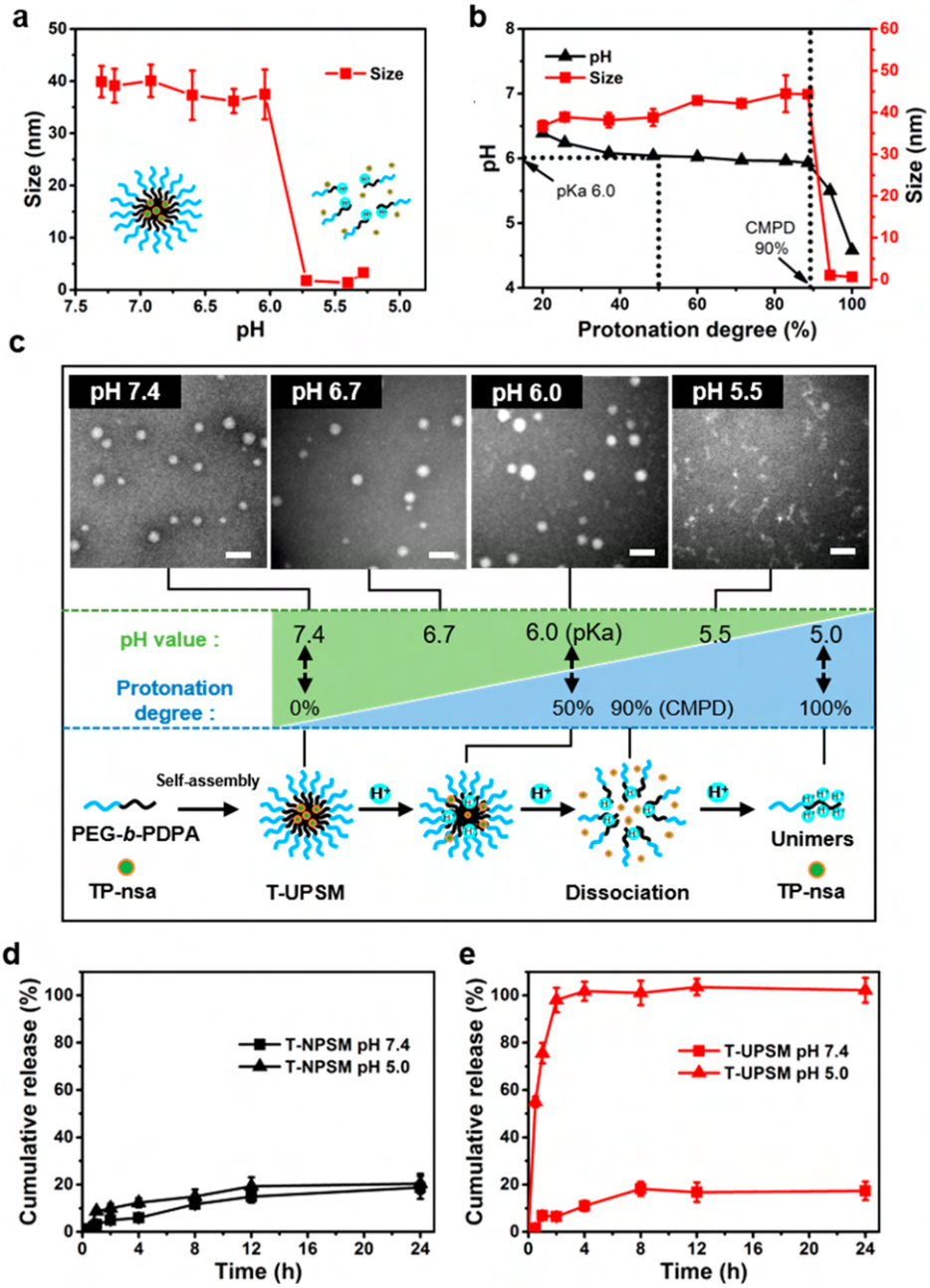

Figure 3. pH-responsive behavior and drug release profiles of T-UPSM and T-NPSM. (a) Change in the size of T-UPSM with HCl (0.1 M) titration. T-UPSM remain as micelles at pH above 6.0 and dissociate into unimers below pH 6. (b) Change in the pH and particle size of T-UPSM (1 mg/mL) as a function of protonation degree. T-UPSM remain as micelles until 90% protonation. The dotted horizontal line indicates the apparent pK_a of T-UPSM (pH 6.0), where 50% of amines are protonated. The left and right dotted vertical line indicates 50% protonation and the critical micelle protonation degree (CMPD) of T-UPSM at 90%, respectively. (c) Representative TEM images of T-UPSM at various pH values. Scale bar: 50 nm. Schematic illustration of pH titration and the protonation process of T-UPSM is shown along with the TEM images. When the protonation degree is below the CMPD, the PEG-*b*-PDPA polymer becomes hydrophobic enough to self-assemble into micelles. Otherwise, the polymer will be protonated and water-soluble, and T-UPSM will dissociate into unimers and rapidly release the payloads. Release profiles of TP-nsa at pH 5.0 and 7.4 from (d) T-NPSM and (e) T-UPSM in 24 h.

DQ-BSA was degraded by PANC-1 cells under fed condition, while significantly increased DQ-BSA degradation was observed under starved condition (Figure 4c,d). The high Pearson's correlation coefficients in each group confirmed the colocalization of DQ-BSA within lysosomes (Figure 4e). Importantly, UPSM (46 μM or 1 mg/mL) but not NPSM abrogated the degradation of DQ-BSA under starved condition (Figure 4c,d), indicating that UPSM were able to inhibit lysosomal catabolism under starved condition through a pH buffering effect. We further used conventional lysosomotropic agents CQ (46 μM) and BafA1 (200 nM) as positive controls. Based on the comparison of the mean DQ-BSA fluorescence intensity, UPSM are more potent than CQ or BafA1 in inhibiting the lysosomal degradation of albumin under starved condition (Figure 4c,d). Additionally, we compared the kinetics of lysosomal catabolism inhibition by UPSM, CQ, or BafA1, which indicated that UPSM could inhibit lysosomal catabolism for at least 6 h, which is longer than CQ or BafA1

DOI: 10.1021/acsnano.8b08246
ACS Nano 2019, 13, 4049−4063

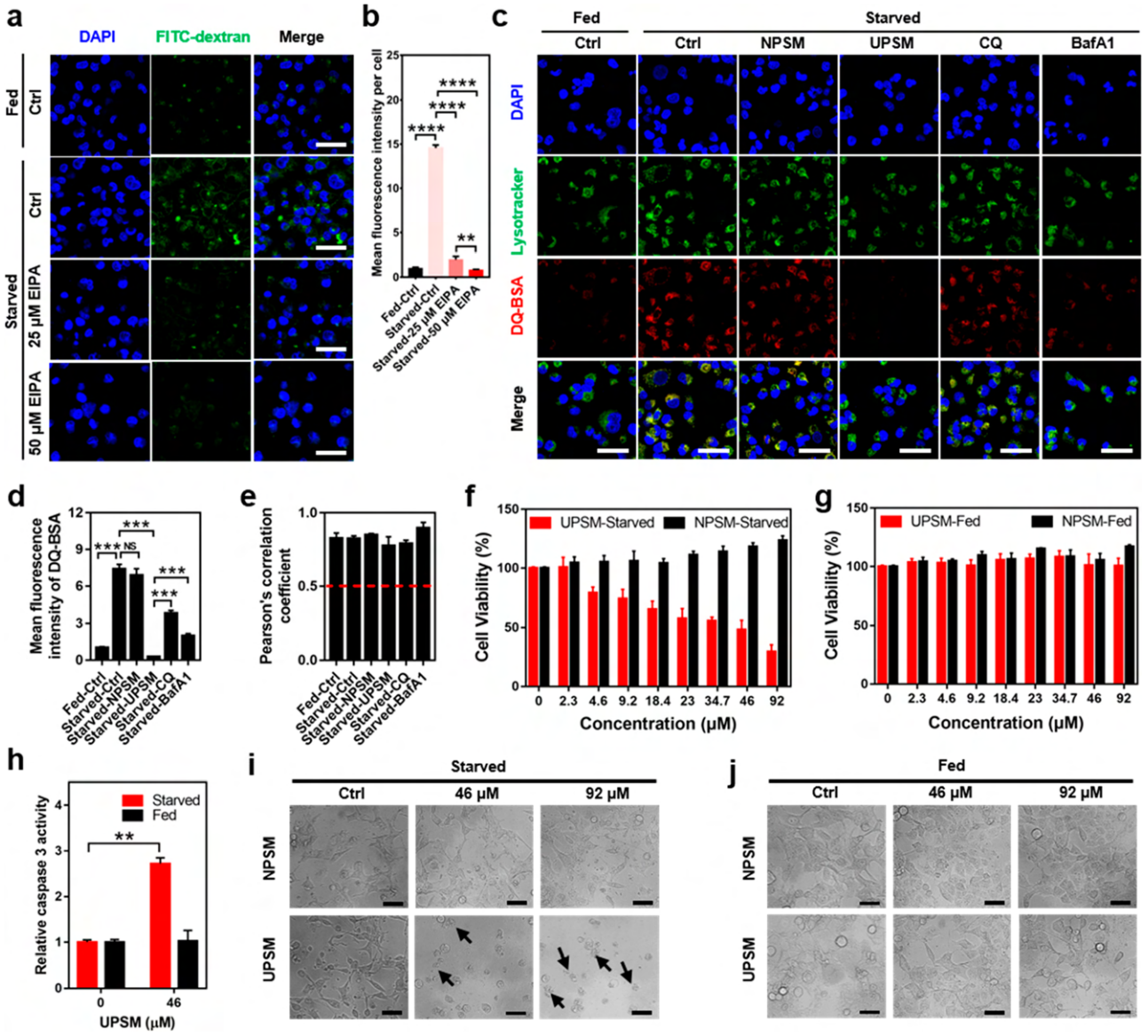

Figure 4. Cell uptake, viability, and lysosomal degradation of DQ-BSA of PANC-1 cells after various treatments. (a) Macropinocytosis of PANC-1 cells after incubation with FITC-dextran (1 mg/mL) (with or without EIPA) for 1 h under fed (complete medium with 10% FBS) and starved (DMEM, FBS-free) conditions. Uptake of FITC-dextran was observed by confocal laser scanning microscopy (CLSM). Scale bar: 50 μm. (b) Quantification of macropinocytosis in (a). Error bars indicate mean ± SD with at least 300 cells in random fields. (c) Representative CLSM images of lysosomal degradation of DQ-BSA in PANC-1 cells treated with NPSM (46 μM), UPSM (46 μM), CQ (46 μM), and BafA1 (200 nM) for 1 h. Scale bar: 50 μm. (d) Quantification of mean fluorescence intensity of degraded DQ-BSA in cells shown in (c). Data are represented as mean ± SD (n = 3 fields of view with >20 cells each). NS, not significant, ***P < 0.001. (e) Pearson's correlation coefficient analysis of the colocalization between DQ-BSA and LysoTracker in PANC-1 cells by ImagePro Plus. Data are represented as mean ± SD, n = 4 per group. The red dashed line indicates 50% colocalization. Viability of PANC-1 cells after incubation with increasing concentrations of UPSM or NPSM under (f) starved and (g) fed conditions for 48 h. (h) Relative caspase-3 activity of PANC-1 cells under starved or fed condition measured after 48 h of incubation with 46 μM UPSM using a caspase-3 detection kit. Representative bright field images of PANC-1 cells treated with UPSM and NPSM (0, 46, and 92 μM) under starved (i) or fed (j) condition. The black arrows indicate apoptotic cells with folded and pyknotic morphology. Scale bar: 50 μm.

(Figure S9a–c). The above results confirmed that UPSM inhibited lysosomal catabolism in PANC-1 cells more efficiently, both in potency and in time duration, than conventional lysosomotropic agents.

UPSM Kill PANC-1 Cells through Apoptosis under Starved Condition. We examined the viability of PANC-1 cells after UPSM treatment under fed or starved conditions. As expected, UPSM at 92 μM reduced PANC-1 cell viability by nearly 75% under starved condition, whereas no change in cell viability was observed by NPSM at the same concentration (Figure 4f). This result indicated that UPSM but not NPSM inhibited PANC-1 cell growth, which again could be attributed to the disruption of lysosomal catabolism by UPSM. In contrast to the starved condition, neither UPSM nor NPSM reduced cell viability under fed condition (Figure 4g), which was not surprising since NPSM (or PEG-*b*-PLA) is biocompatible (Figure 4f), while the pH buffering effect by UPSM became negligible since cell uptake under fed condition was largely suppressed (Figure 4a,b). The selective inhibition of tumor cell growth under starved condition might expand the

DOI: 10.1021/acsnano.8b08246
ACS Nano 2019, 13, 4049–4063

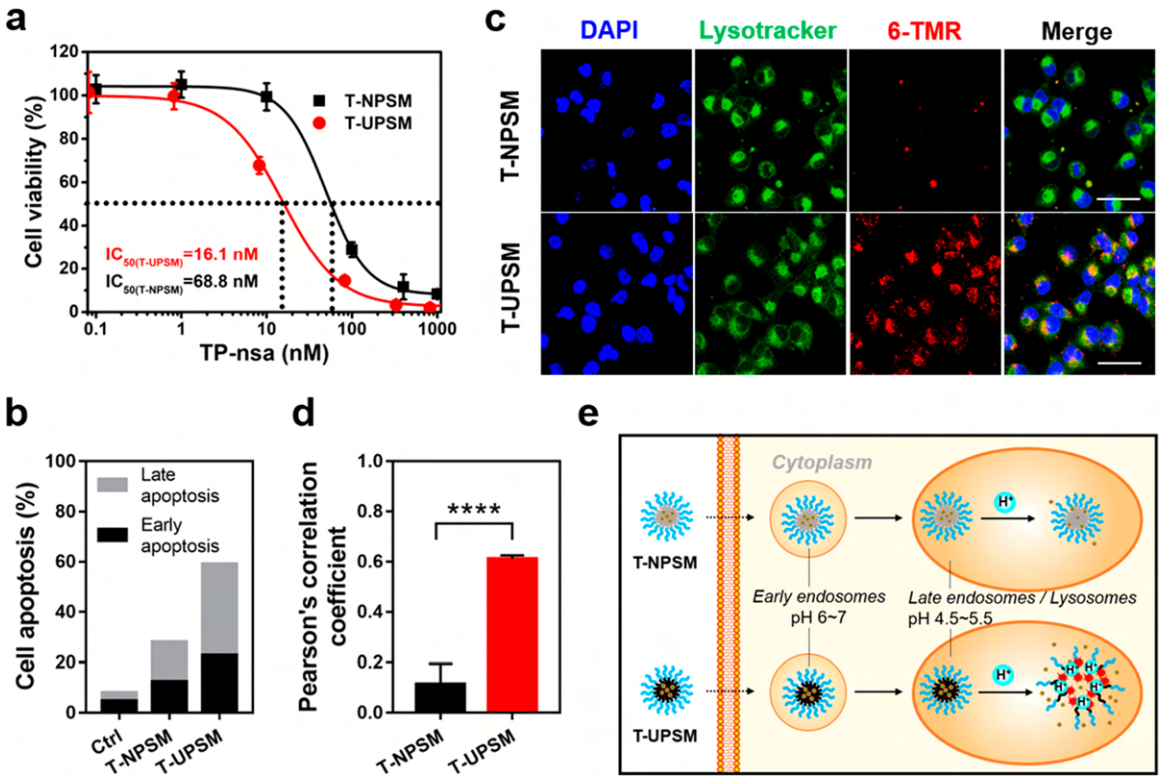

Figure 5. Cytotoxicity and intracellular trafficking of T-UPSM and T-NPSM in PANC-1 cells. (a) Viability of PANC-1 cells after treatment with T-NPSM or T-UPSM (with 20 U/mL PLE) for 72 h under fed condition. The dotted vertical lines indicate the IC_{50} of T-UPSM (16.1 nM) and T-NPSM (68.8 nM), respectively. (b) Percentage of apoptotic PANC-1 cells after treatment with 50 nM T-NPSM or T-UPSM (with 20 U/mL PLE) for 48 h under fed condition detected by flow cytometry. (c) Representative CLSM fluorescent images of intracellular trafficking study of fluorescence-labeled T-UPSM and T-NPSM. Scale bar: 50 μm. (d) Pearson's correlation coefficient analysis of the colocalization between dye-labeled micelles and lysosome markers in PANC-1 cells by ImagePro Plus. Error bars indicate mean ± SD; $n = 6$ per group. ****$P < 0.0001$. (e) Schematic illustration of the distinct intracellular behaviors of T-NPSM and T-UPSM.

therapeutic window, since the *in vivo* tumor microenvironment of pancreatic cancers is nutrient poor.[8,13,14,19,50]

We then evaluated cell apoptosis under starved condition and measured caspase-3 activity[31] of PANC-1 cells after treatment with UPSM for 48 h. Indeed, UPSM alone enhanced the activation of caspase-3 under starved condition than fed condition (Figure 4h). The bright field images of PANC-1 cells after UPSM treatment also confirmed cell apoptosis, where the cells gradually became folded and pyknotic under starved condition (Figure 4i, lower panel).[51,52] Consistent with the cell viability assays, no obvious change in cell morphology was observed after NPSM treatment under starved condition (Figure 4i, upper panel) or treatment with either of the micelles under fed condition (Figure 4j). Altogether, these results revealed that UPSM reduced viability of PANC-1 cells by inducing apoptosis under starved condition, which can be attributed to the disruption of lysosomal catabolism (Figure 4c–e).

We further investigated several lysosomal amino acids after treatment with UPSM or NPSM for 24 h under starved condition, to evaluate the influence of UPSM on lysosomal catabolism and generation of metabolite intermediates. It has been known that amino acids in lysosomes are regulated by lysosomal pH gradient or nutrient conditions.[27] Indeed, the profiling results demonstrated that UPSM significantly reduced glutamates and prolines in lysosomes, which were vital amino acids for PDAC growth especially in nutrient-depletion condition,[13,53–55] while the other four amino acids showed a minor decrease (Figure S9d). In contrast, NPSM showed little impact on amino acid production compared with vehicle (Figure S9d). These data confirmed that UPSM, but not NPSM, effectively disrupted lysosomal catabolism and reduced the generation of vital amino acids that may contribute to PANC-1 cell survival.

pH-Triggered Rapid Drug Release from T-UPSM Enhanced Cytotoxicity Compared with T-NPSM. We showed earlier that T-UPSM released drug rapidly below pH 6 (Figure 3a–c,e). We hypothesized that rapid drug release from T-UPSM, triggered by acidic lysosomal pH, would enhance drug cytotoxicity compared with a slower drug release from T-NPSM. Since the pH buffering effect itself by internalized UPSM could significantly inhibit the growth of cells cultured in starved condition (Figure 4f), here we cultured cells in fed condition to minimize the influence of pH buffering (Figure 4g) while allowing the assessment of pH-triggered drug release on cell viability. Indeed, T-UPSM were more potent than T-NPSM to inhibit PANC-1 cell growth (Figure 5a), with an IC_{50} value (16.1 nM) less than 4-fold lower than that of T-NPSM (68.8 nM). Moreover, the apoptosis assay of PANC-1 cells using flow cytometry revealed that T-UPSM induced about 2-fold more early and late apoptosis than T-NPSM at the same drug concentrations (Figure 5b and Figure S11).

To further confirm that the enhanced cytotoxicity of T-UPSM was due to pH-triggered drug release, we performed an intracellular trafficking study with fluorescence-labeled T-UPSM and T-NPSM. The red fluorescent dye 6-tetramethylr-

DOI: 10.1021/acsnano.8b08246
ACS Nano 2019, 13, 4049–4063

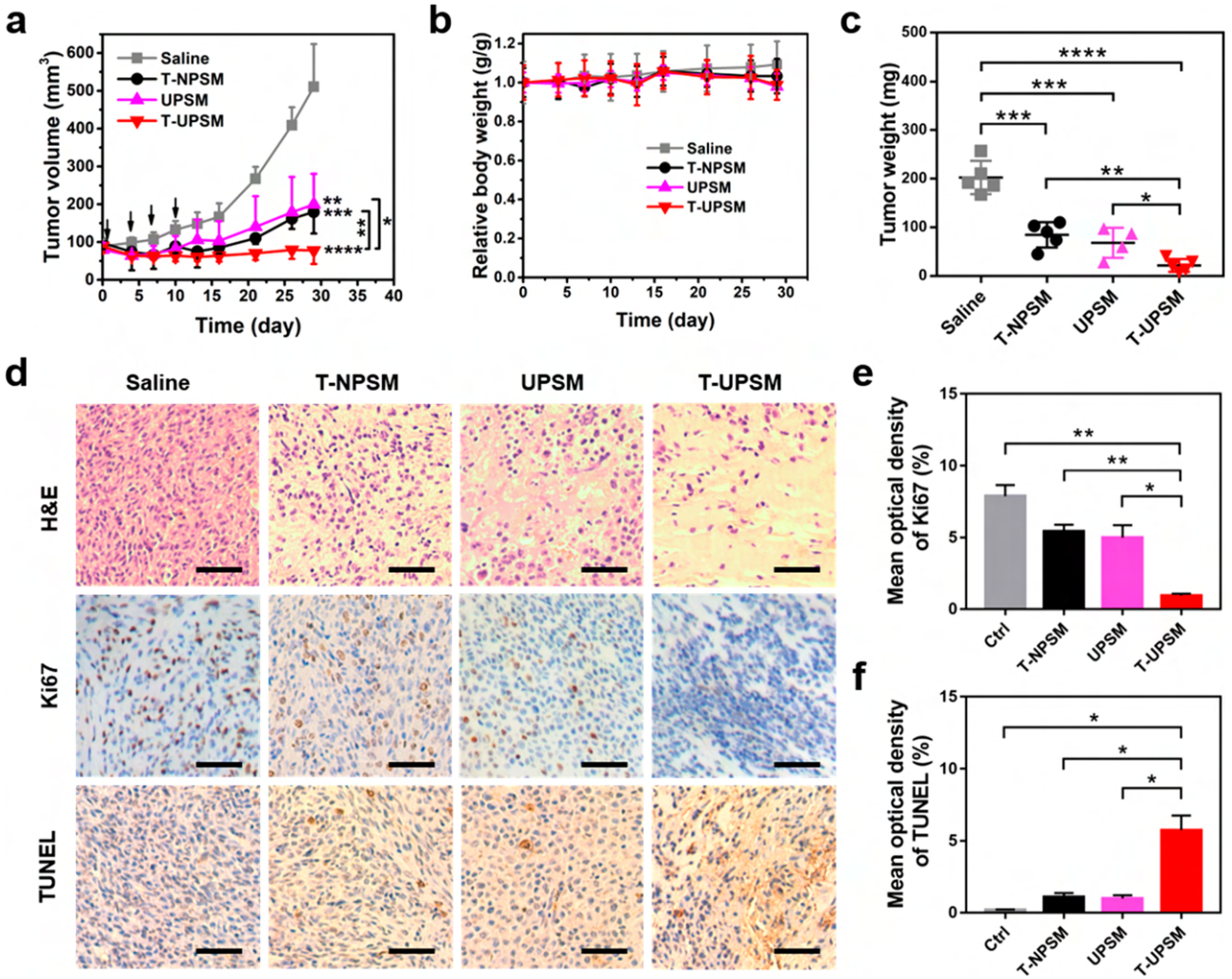

Figure 6. Antitumor efficacy in a subcutaneous KRAS mutant PANC-1 cell-derived xenograft mouse model. (a) Change in tumor volume over time for different treatment groups (n = 5). The black arrows indicate the days of injection. (b) Relative changes in mouse body weight. (c) Final tumor weights at the end of the experiment. (d) Representative images of histological (H&E, Ki67, and TUNEL staining) analyses of tumor sections. Scale bar: 50 μm. Quantification analysis of (e) mean density of Ki67 and (f) TUNEL staining by ImagePro Plus (n = 6 random fields). In (a), (c), (e), and (f), data are presented as the mean ± SD (*P < 0.05, **P < 0.01, ***P < 0.001, ****P < 0.0001, two-tailed t test).

hodamine (6-TMR) is chemically conjugated to the hydrophobic segment of copolymers (*i.e.*, −PDPA and −PLA). Consequently, the fluorescence of both micelles was quenched due to the close proximity of fluorophores encapsulated in the micelle core.[42,56] Upon micelle dissociation, the fluorescent dyes were separated and the fluorescence intensity increased. Lysosomes were labeled with LysoTracker to track the intracellular localization of both micelles. Almost all the cells treated with T-UPSM were labeled with red fluorescence after 1 h, whereas only weak red fluorescence was found in the T-NPSM group (Figure 5c). Moreover, Pearson's correlation coefficient analysis revealed that the red fluorescence was mainly colocalized with green signals in the T-UPSM group, indicating the lysosomal drug release (Figure 5d). These results demonstrated that T-UPSM dissociated and rapidly released the payload in lysosomes in response to the acidic lysosomal pH. After being released into lysosomes, TP-nsa could be hydrolyzed into TP and induce cell apoptosis by targeting HSP70 and XPB.[32,33] The intracellular trafficking study clearly indicated that T-UPSM improved the lysosomal drug release compared with T-NPSM and thus enhanced cytotoxicity toward PANC-1 cells (Figure 5a). The cartoon in Figure 5e illustrates the intracellular trafficking of both micelles from endosomes to lysosomes. T-UPSM remained mostly intact in early endosomes (pH 6−7),[45] while they dissociated and rapidly released drugs in late endosomes or lysosomes (pH 4.5−5.5),[45,46] accompanied by the emitted fluorescence from the dissociated 6-TMR dyes.

T-UPSM Inhibited Tumor Growth in KRAS Mutant PDAC Mouse Models. An *in vivo* antitumor efficacy study was performed using a subcutaneous KRAS mutant PANC-1 cell-derived xenograft mouse model. The tumor-bearing mice were randomly divided into four groups (n = 5), *i.e.*, saline (control), UPSM (10 mg/kg of PEG-*b*-PDPA), T-NPSM (0.3 mg/kg of TP), and T-UPSM (0.3 mg/kg of TP, the dose of polymer was equivalent to UPSM). TP was not included because we did not intend to compare the therapeutic efficacy of drug-loaded micelles with prototype drug TP in this experiment, although TP has been investigated in our preliminary study and by others to show no significant inhibition effect on *in vivo* tumor growth.[57,58] Interestingly, the inhibition of tumor growth by UPSM alone was comparable to

DOI: 10.1021/acsnano.8b08246
ACS Nano 2019, 13, 4049−4063

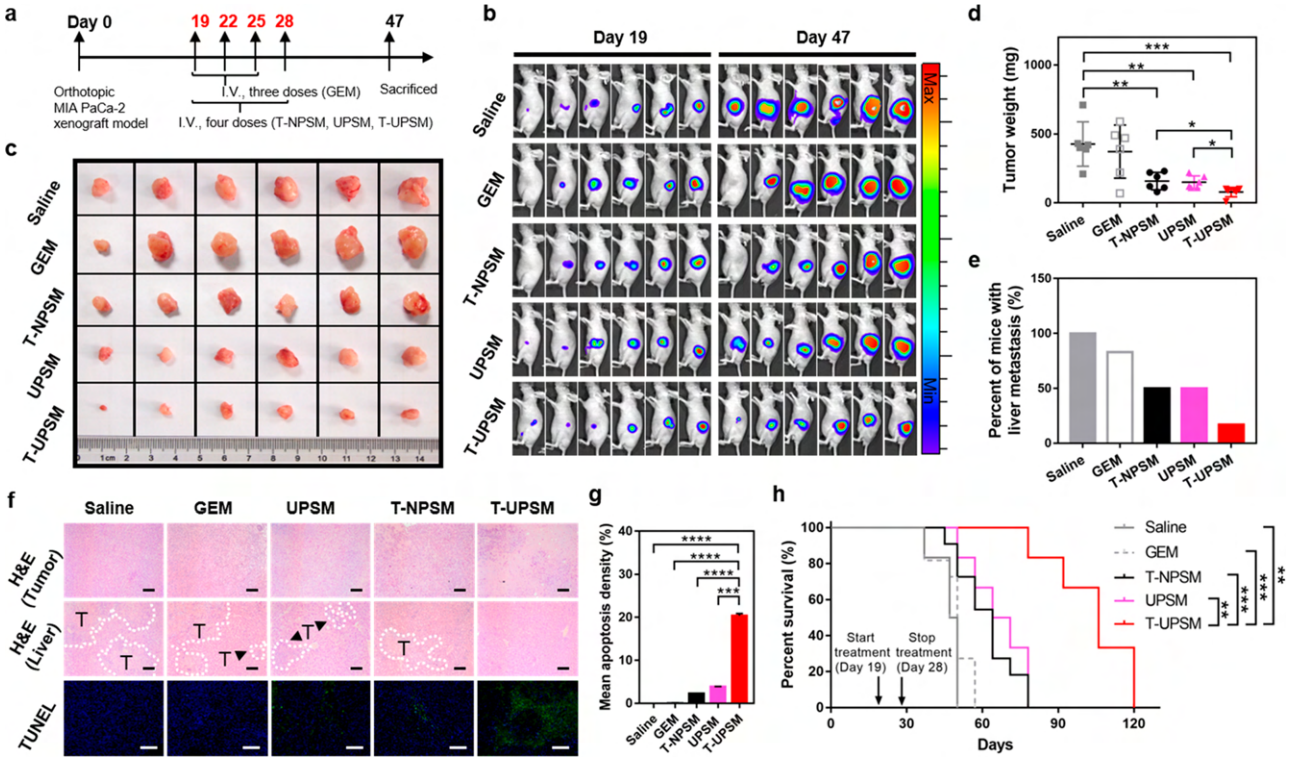

Figure 7. Antitumor efficacy in an orthotopic KRAS mutant MIA PaCa-2 cell-derived xenograft mouse model. (a) Scheme of treatment of different formulations. Mice were intravenously administrated with either GEM (50 mg/kg) for three doses or T-NPSM (0.3 mg/kg), UPSM (10 mg/kg), and T-UPSM (0.3 mg/kg) every other day for a total of four doses. (b) Bioluminescence images of anesthetized mice before (day 19) and after (day 47) treatments. Day 0 was designated as the day after injection of MIA PaCa-2-luc cells. (c) *Ex vivo* tumor pictures and (d) tumor weights after mice were randomly selected and sacrificed at the end of the experiment. Data are presented as the mean ± SD (n = 6). *P < 0.05, **P < 0.01, ***P < 0.001, two-tailed t test. (e) Percentages of liver metastasis in different treatment groups. (f) Representative images of *ex vivo* histological (H&E and TUNEL staining) analyses of tumor sections. The areas surrounded with a white dotted line (marked with T) represent metastatic tumors. Scale bar: 50 μm. (g) Quantity analysis of apoptosis density in TUNEL staining by ImagePro Plus (n = 6 random fields). Data are presented as the mean ± SD (*P < 0.001, ****P < 0.0001, two-tailed t test). (h) Kaplan–Meier survival curve of orthotopic xenograft models (n = 6 for saline, UPSM, and T-UPSM, n = 11 for GEM and T-NPSM) after treatment with the above formulations. Statistical significance for survival analysis was calculated by the log-rank test: **P < 0.01, ***P < 0.001.**

that of T-NPSM (Figure 6a), demonstrating the potent antitumor efficacy of UPSM *in vivo*, presumably due to its strong lysosomal pH buffering effect and the starved tumor microenvironment.[8,13,14,19,50] The *in vivo* antitumor efficacy of T-UPSM and T-NPSM (Figure 6a) was consistent with the *in vitro* studies that rapid lysosomal drug release from T-UPSM enhanced cytotoxicity compared with T-NPSM (Figure 5). Importantly, tumor growth was almost completely inhibited by T-UPSM, but not T-NPSM (Figure 6a), indicating that T-UPSM could enhance suppression of KRAS mutant tumor growth, which could be attributed to the combination effect of lysosomal pH buffering and rapid lysosomal drug release. Inconspicuous changes in body weight in all groups demonstrated no significant toxicity at the tested doses (Figure 6b). In fact, we have evaluated the systemic toxicity of these micelles *in vivo* in male BALB/C mice, and no significant toxicity was detected with UPSM doses up to 60 mg/kg (administrated four doses every other day). The maximum tolerated doses (MTD) of T-NPSM and T-UPSM were both found to be 2.4 mg/kg, which was 2-fold higher than the parent drug triptolide (Figure S12). The comparison of tumor weight at the completion of the experiment also confirmed that T-UPSM were more efficient than T-NPSM or UPSM in inhibiting KRAS mutant tumor growth (Figure 6c).

We further assessed the cell proliferation and apoptosis by *ex vivo* histological analyses of tumor sections. It was obvious that there were much more dead tumor cells in the T-UPSM group than the other groups (Figure 6d, H&E). The Ki67 staining indicated that T-UPSM efficiently inhibited proliferation of tumor cells (Figure 6d,e), and TUNEL staining further confirmed that T-UPSM induced the most pronounced apoptosis of tumor cells (Figure 6d,f). These data strengthened the *in vitro* findings that T-UPSM efficiently reduced cell viability by inducing apoptosis of PANC-1 cells (Figure 5a,b). Therefore, T-UPSM displayed synergistic antitumor efficacy in the subcutaneous KRAS mutant PDAC mouse model.

T-UPSM Suppressed Tumor Growth and Metastasis and Significantly Prolonged the Survival Time of the Orthotopic KRAS Mutant PDAC Model. The orthotopic xenograft model is considered to be more clinically relevant due to its physiological and histological similarities with the desmoplastic human pancreatic cancer,[59] especially with regard to tumor microenvironment and metastasis.[60] Therefore, we further investigated the antitumor efficacy of the above formulations in a luciferase-expressed, KRAS mutant MIA PaCa-2 cell-derived orthotopic mouse model. The first-line PDAC chemotherapy drug gemcitabine (GEM) was used as a positive control (Figure 7a). The *in vivo* bioluminescence images of mice after treatment (day 47) showed that GEM had

DOI: 10.1021/acsnano.8b08246
ACS Nano 2019, 13, 4049–4063

poor tumor inhibition effect on the orthotopic PDAC model (Figure 7b), similar to a previous report.[61] Strikingly, T-UPSM suppressed the growth of orthotopic tumors more efficiently than either T-NPSM or UPSM, which also inhibited tumor growth (Figure 7b), indicating the synergistic tumor inhibition effect of T-UPSM. The *ex vivo* tumor pictures and final tumor weights also confirmed such enhanced tumor inhibition effect of T-UPSM (Figure 7c,d). In addition, compared with other treatments, T-UPSM markedly suppressed tumor metastasis to the liver (Figure S10), supported by histological examination of the livers (Figure 7f). We also assessed the cell proliferation and apoptosis in orthotopic tumor tissues. T-UPSM induced the most significant cell death, as shown in H&E staining images, and TUNEL staining results revealed that T-UPSM induced more cell apoptosis than other treatments (Figure 7f,g). Importantly, the KRAS mutant PDAC mouse model treated with T-UPSM achieved the longest median survival time (106 days) compared with GEM (50 days), T-NPSM (64 days), and UPSM (67.5 days) (Figure 7h). These data corroborated that T-UPSM efficiently inhibited KRAS mutant PDAC growth by increased cytotoxicity and suppressed tumor metastasis, thus enhancing anti-PDAC efficacy and prolonging the survival of PDAC tumor bearing mice.

DISCUSSION

Over 30% of all human cancers, including ∼95% of PDAC, ∼45% of colorectal, and ∼31% of lung cancers, are KRAS driven, which remain the most intractable cancers.[5,62] Results from this study showed that lysosomal pH buffering by UPSM could efficiently disrupt lysosomal catabolism and inhibit the growth of KRAS mutant PDAC. Additionally, pH-triggered lysosomal drug delivery enhanced cytotoxicity against PDAC. The UPSM therapeutic platform achieved synergistic anti-tumor efficacy in preclinical KRAS mutant PDAC models as illustrated in Scheme 1.

Our T-UPSM system was different from the previous pH-sensitive nanoplatform in the following aspects: first, most nanocarriers have no pharmacological effects despite their pH-stimuli response characteristics,[63−65] whereas UPSM alone could inhibit cancer cell growth by blocking lysosomal catabolism through strong pH buffering. In fact, T-UPSM were designed to target the KRAS-enhanced macropinocytosis and lysosomal acidification in PDAC cells, rather than the acidic tumor microenvironmental pH (pHe), like most of the pH-sensitive nanoplatform systems.[63−65] Second, unlike conventional pH-sensitive polymers (*e.g.*, dendrimers, chitosan, polyethylenimine, or poly(L-lysine)), the UPSM copolymers undergo catastrophic phase transitions (*i.e.*, micellization) at their apparent pK_a (Figure 3a,b). Below the critical micellization protonation degree (90% for the current PEG-*b*-PDPA copolymer), UPSM copolymers undergo a binary all-or-nothing protonation phenotype where the copolymers inside micelles are neutral and the unimers in solution are highly protonated. This bistable state solution is a result of molecular cooperativity of protonation-induced phase transitions, and the Hill coefficient of 51 in pH cooperativity for a representative UPS block copolymer is by far the largest reported in the literature.[34] In the micelle form, the neutral PDPA segment in the micelle core created a hydrophobic environment for efficient drug encapsulation, as demonstrated by the almost quantitative loading efficiency of triptolide prodrugs (82.0 ± 3.5%). Upon micelle uptake in the endocytic organelles of cancer cells, acidification of lysosomal luminal pH will reach the apparent pK_a of UPSM copolymers. Absorption of the protons by the tertiary amine groups at the threshold pH renders two consequences: first, the luminal pH of the endosome/lysosome is buffered until all the UPSM copolymers are protonated; second, protonation of the UPSM copolymers leads to micelle dissociation and immediate drug release. This simultaneous buffering of organelle pH and pH-triggered drug release synergize the blocking of lysosomal catabolism with drug-induced cell cytotoxicity for the synergistic treatment of KRAS mutant pancreatic cancer.

Previous studies have shown that mutant KRAS is responsible for elevated macropinocytosis of serum albumin and autophagy of intracellular proteins for cell growth and survival under nutrient-deprived conditions.[3,5] Our recent multicolored pH barcode imaging study further illustrated mutant KRAS is responsible for accelerated organelle acidification of lysosomes,[24] which corroborates metabolic reprograming of lysosomes in the KRAS mutant cancer cells. Lysosomotropic agents such as hydroxychloroquine have been tested in patients to treat various cancers including PDAC.[18,28] Compared to membrane-permeable hydroxychloroquine, UPSM can only be taken up through endocytosis, thereby targeting the metabolic vulnerabilities of the KRAS mutant cancers. Furthermore, UPSM have much stronger pH buffering capacity at a specific pH threshold over chloroquine (30- to 300-fold higher),[31] which improves the pharmacologic potency and precision. In this study, we chose a UPSM copolymer with maximal pH buffering capacity at pH 6.0. Previous studies have shown that blocking of luminal pH above 5.0 not only blocks lysosomal catabolism but also inhibits the mTOR signaling pathway, leading to cell growth inhibition and apoptosis in cell culture.[31] Results from this study demonstrate that UPSM alone is able to inhibit tumor growth and prolong animal survival in both PDAC tumor models (Figures 6 and 7). Incorporation of a cytotoxic agent in the UPSM further synergizes with blocking of lysosome metabolism, which leads to significantly improved survival of animals.

Notably, although the orthotopic xenograft models are often used for pancreatic cancer research and can reflect the tumor microenvironment and metastasis more concisely than the subcutaneous xenograft model, they are not developed spontaneously as the genetically engineered LSL-$Kras^{G12D/+}$;LSL-$Trp53^{R172H/+}$;Pdx-1-Cre (KPC) mouse model,[66] which would be more clinically relevant and translational.[67] Further studies using T-UPSM in the KPC model or even combining with other treatments are worth more investigation. Besides, it is well known that the tumor microenvironment in PDAC is really complicated due to the abundant stroma that includes cancer-associated fibroblasts (CAFs), extracellular matrix, suppressor immune cells, and tumor-associated macrophages (TAMs),[2,9,68] which may impair drug delivery to PDAC. In this study, we mainly focused on KRAS mutant cancer cells and the abnormal cell metabolism. More comprehensive strategies to overcome the barrier of stroma are necessary, and some separate studies to target CAFs or extracellular matrix using UPSM-based therapies in the KPC model are ongoing in our lab. Altogether, our proof-of-concept study offers an exciting alternative to target the metabolic vulnerability of KRAS mutant PDAC where conventional chemotherapy and checkpoint inhibitor therapy have shown inadequate efficacy.

DOI: 10.1021/acsnano.8b08246
ACS Nano 2019, 13, 4049−4063

CONCLUSIONS

In this study, we report a UPSM platform with strong lysosomal pH buffering capacity and pH-triggered rapid drug release property for the treatment of KRAS mutant pancreatic cancer. Our results demonstrate the capability of the UPSM platform as a targeted therapy against KRAS mutant PDAC cancers that have been elusive to the small molecular drugs. The UPSM strategy exploits the elevated macropinocytosis and accelerated lysosome metabolism that are innate to mutant KRAS, a prevalent biomarker in >95% of PDAC tumors. Compared to clinically used lysosomotropic drugs such as chloroquine, UPSM allowed a much higher potency and more precise targeting of organelle pH with significantly improved inhibition of tumor growth. The binary all-or-nothing protonation phenotype of the UPSM nanoparticles synchronizes pH buffering with rapid drug release inside endosomes/lysosomes. Data using a representative cytotoxic drug, triptolide, a traditional Chinese herbal medicine that targets HSP70[32] and XPB transcription,[33] showed enhanced cytotoxicity and synergistic antitumor efficacy in preclinical PDAC models. This proof-of-concept study suggests that drug-loaded UPSM can be a promising therapeutic strategy against KRAS-transformed cancers such as PDAC.

EXPERIMENTAL SECTION

Materials. TP was obtained from Chengdu Biopurify (Chengdu, China). Naphthalene sulfonamide (nsa) was purchased from Alfa Aesar (Beijing, China). 1-Ethyl-3-(3-(dimethylamino)propyl)-carbodiimide hydrochloride (EDC·HCl) was purchased from Shanghai Medpep (Shanghai, China). 4-(Dimethylamino)pyridine (DMAP) was purchased from Aladdin (Shanghai, China). Trimethylamine (TEA) was purchased from Xilong Scientific (Guangdong, China). PEG-*b*-PLA was supplied by Daigang Biomaterial (Jinan, China), and fluorescence-labeled PEG-*b*-PLA (PEG-*b*-PLA-TMR) was synthesized by conjugating PEG-*b*-PLA-NH_2 with 6-carboxytetramethylrhodamine succinimidyl ester (6-TMR) (Lynnchem, Xi'an, China). PEG-*b*-PDPA and PEG-*b*-PDPA-TMR were synthesized according to reported procedures.[56] Gemcitabine was purchased from Nanjing Jingrui Jiuan Bio-Technology (Nanjing, China). All standard amino acids (proline, alanine, glutamic acid, leucine, tyrosine, and phenylalanine; ≥98% HPLC grade) were purchased from Sigma-Aldrich (Shanghai, China). All organic solvents were of analytical grade or LC/MS grade.

Cells, Culture Medium, and Biological Reagents. PDAC cells, including PANC-1 and MIA PaCa-2, were obtained from the American Type Culture Collection (ATCC). DAPI, CCK-8 kit, and caspase 3 kit were purchased from Beyotime (Shanghai, China). FITC-dextran (15 kDa), annexin V-FITC, and propidium iodide (PI) were purchased from Sigma (Shanghai, China). EIPA was purchased from MCE (NJ, USA). DQ-BSA Red and LysoTracker Deep Red were purchased from Invitrogen (CA, USA). FBS was obtained from Corning (Manassas, VA, USA). DMEM, (basic (1×)), trypsin-EDTA, phosphate-buffered saline (PBS), and streptomycin/penicillin (S/P) antibiotics were supplied by Thermo Fisher Scientific (Shanghai, China). Lysosome isolation kit was purchased from BestBio Company (Shanghai, China). CQ was purchased from Bide Pharmatech Ltd. (Shanghai, China). Bafilomycin A1 (BafA1) was purchased from Toronto Research Chemicals (Toronto, Canada). Generally, cells were cultured in DMEM with 10% (v/v) FBS and 1% (v/v) S/P at 37 °C under a 5% CO_2/95% humidified atmosphere. For the starved (nutrient-deprived) condition, cells were precultured in DMEM (37 °C, FBS-free) for 12 h before experiments and then cultured in DMEM (37 °C, FBS-free). For the fed (nutrient-supplied) condition, cells were cultured in DMEM (37 °C, 10% FBS). MIA PaCa-2-luc cells (transfected with a plasmid encoding for luciferase) were kindly provided by Dr. David C. S. Huang (University of Melbourne). D-Luciferin was purchased from Gold Biotechnology (St Louis, MO, USA). Paraformaldehyde (PFA) was purchased from Solarbio (Beijing, China).

Synthesis and Characterization of TP-Naphthalene Sulfonamide. TP (0.72 g, 2 mmol) and succinic anhydride (1.0 g, 0.01 mol) were dissolved in 2 mL of anhydrous CH_2Cl_2; then DMAP (1.2 g, 0.01 mol) and TEA (2.06 g, 0.01 mol) were added and reacted at room temperature under N_2 for 1 h. The reaction was monitored using thin layer chromatography (TLC). The resulting mixture was washed with water and HCl (0.1 M) to remove the unreacted reactant, and the organic extract was dried over sodium sulfate and evaporated to give compound **2**. A mixture of compound **2** (0.46 g, 1 mmol), naphthalene sulfonamide (0.249 g, 1.2 mmol), DMAP (0.183 g, 1.5 mmol), and EDC·HCl (0.230 g, 1.2 mmol) in CH_2Cl_2 was stirred overnight at room temperature to yield compound **3** (TP-nsa). Purification was performed by silica gel column chromatography. The structures of compounds were confirmed by ^{1}H NMR, ^{13}C NMR, and Q-TOF. The NMR spectra were obtained in $CDCl_3$ using tetramethylsilane (TMS) as the internal reference on a Bruker 400 MHz NMR spectrometer. The characterization of TP-nsa is as follows:

^{1}H NMR (TMS, $CDCl_3$, ppm): 0.77 (d, J = 6.8 Hz, 3H), 0.85 (d, J = 7.2 Hz, 3H), 1.02 (s, 3H), 1.56 (dd, J = 12.8 Hz, J = 5.6 Hz, 1H), 1.81−1.90 (m, 2H), 2.12−2.18 (m, 2H), 2.57−2.78 (m, 5H), 3.47 (d, J = 5.2 Hz, 1H), 3.58 (d, J = 2.8 Hz, 1H), 3.90 (d, J = 2.8 Hz, 1H), 4.67 (m, 2H), 5.04 (s, 1H), 7.60−7.69 (m, 2H), 7.91 (d, J = 8.0 Hz, 1H), 7.96−8.03 (m, 3H), 8.67 (d, J = 1.6 Hz, 1H), 9.72 (s, 1H), as shown in Figure S2; ^{13}C NMR (TMS, $CDCl_3$, ppm): 13.8, 14.3, 16.4, 17.1, 17.4, 21.1, 23.3, 27.6, 29.2, 29.8, 31.5, 35.7, 40.3, 54.8, 56.1, 59.8, 60.5, 61.4, 63.2, 64.2, 70.2, 71.9, 122.9, 125.5, 127.7, 127.9, 129.2, 129.4, 129.7, 130.5, 135.4, 135.6, 160.2, 170.0, 171.1, 173.5, as shown in Figure S3; Q-TOF MS m/z: $[M]^+$ calculated for $C_{34}H_{35}NO_{10}S$, 854.46, found: 672.18 (M + Na^+), as shown in Figure S4.

Preparation of Blank or Drug-Loaded NPSM and UPSM. Blank or drug-loaded PEG-*b*-PLA micelles (NPSM or T-NPSM) were prepared using a previously reported thin-film evaporation and sonication method.[38] Briefly, PEG-*b*-PLA copolymer (with or without drug) was dissolved in acetonitrile and evaporated using a rotary evaporator at 60 °C to form a thin film. The film was hydrated by 5 mL of H_2O (60 °C) and sonicated for 5 min to obtain the final micelle solution. Blank or drug-loaded PEG-*b*-PDPA micelles (UPSM or T-UPSM) were prepared using a previously reported method.[56] Briefly, polymer (with or without drug) was dissolved in methanol and then added dropwise to a glass vial containing 4 mL of Milli-Q water under sonication. The solution was then filtrated four times using an ultrafiltration system (MW cutoff 100 kDa, Millipore) under centrifugation (Eppendorf Centrifuge 5810 R, Germany) to remove methanol and finally dispersed into a predetermined volume of PBS.

Characterization of Micelle Size and Morphology. Hydrodynamic diameter (nm) and PDI of micelles were measured by DLS (Malvern Instruments, U.K.) at a scattering light angle of 90°. All experiments were performed in triplicate. Micelle morphology was examined by TEM (FEI Tecnai Spirit Bio TWIN TEM D1297, USA). Briefly, 4 μL of micelle solution was dropped onto 300-mesh carbon-coated copper grids. Negative staining (phosphotungstic acid, pH 6.5) was used to enhance the contrast. After drying for 1 h at room temperature, the micelle images were observed under TEM.

Drug Loading and Encapsulation Efficiency of Micelles. Drug loading (DL) and encapsulation efficiency (EE) of micelles were measured according to the following procedures: 5 mL of T-NPSM or T-UPSM stock solution was filtrated four times using an ultrafiltration system (MW cutoff 100 kDa) under centrifugation at a speed of 3500 rpm at 4 °C to remove the unloaded free drug, and then 5 mL of Milli-Q water was added to prepare the sample solution. An aliquot of 0.2 mL of sample solution was mixed with 0.8 mL of acetonitrile under sonication for 5 min to destroy micelle structure. The sample was then centrifuged at 14 000 rpm for 10 min. A total of 0.7 mL of supernatant was analyzed by HPLC (Shimadzu, Japan) to determine the drug concentration (C_{drug}). The weight of drug in micelles was then calculated by multiplying the concentration by the dilution

DOI: 10.1021/acsnano.8b08246
ACS Nano 2019, 13, 4049−4063

factor. Weight of micelles was calculated by adding the initial polymer weight and the initial drug weight. DL and EE were calculated according to the following equations:

$$\text{Weight of drug in micelles} = (C_{\text{drug}} \times \text{dilution factor}) \times \text{micelle volume} \quad (1)$$

$$\text{DL}\ (\%) = \frac{\text{weight of drug in micelles}}{\text{weight of micelles}} \times 100\% \quad (2)$$

$$\text{EE}\ (\%) = \frac{\text{weight of drug in micelles}}{\text{initial weight of drug in system}} \times 100\% \quad (3)$$

Critical Micelle Concentration Values. CMC values of NPSM and UPSM were measured by a dual-FL fluorescence spectrometer (Horiba Scientific, Japan), utilizing the pyrene I_{372}/I_{383} ratio method.[69,70] Briefly, an equal predetermined amount of pyrene solution in acetone was added to several volumetric flasks and allowed to evaporate using an air pump. Next, different concentrations of polymers were added and the sample was mildly agitated overnight and allowed to reach equilibrium. The excitation wavelength was 339 nm, and the fluorescence intensities at 372 and 383 nm were measured. CMC values were determined from the point of inflection in a plot of I_{372}/I_{383} intensity ratio plotted against the logarithm of polymer concentration.

Titration of UPSM and NPSM. In a typical procedure, 5 mL of micelle solution in water with 154 mM NaCl and indicated polymer concentrations was added into a glass vial. Then 0.1 M HCl was added dropwise into the micelle solution. The pH values of the solution were measured in real time by a Mettler Toledo pH meter under magnetic stirring at room temperature. The titration of UPSM or NPSM was also conducted in biological solutions (10% BSA and 10% FBS solutions) at room temperature.

***In Vitro* Drug Release Study.** The *in vitro* drug release profiles of T-NPSM and T-UPSM were evaluated utilizing centrifugal dialysis methods.[71] PBS solution (0.1 M, with 0.1% Tween 80) with pH 7.4 or pH 5.0 was used for the dissolution study. Briefly, 0.5 mL of micelles was added into centrifuge tubes containing 25 mL of the aforementioned buffer solutions and then stirred in an incubation shaker at 100 rpm at 37 °C. A 1 mL amount of release medium was removed at predetermined time intervals (0.5, 1, 2, 4, 8, 12, 24 h) and replaced with an equal volume of corresponding fresh buffer solution. The release medium was immediately dialyzed using an ultrafiltration system (MW cutoff: 100 kDa) under centrifugation (Eppendorf Centrifuge 5810 R, Germany) to collect released drug solution. The concentration of released drug was determined by HPLC, and the cumulative release percentage (%) was calculated and plotted as a function of time.

Cell Viability Assay. PANC-1 cells were seeded in 96-well plates (Corning, USA) (3×10^3 cells/well) and then cultured overnight in 100 μL of DMEM (10% FBS, 1% P/S). Cells were exposed to various concentrations of drugs or micelles and incubated for predetermined time intervals. Cell viability was determined by a CCK-8 kit according to the manufacturer's instructions. Briefly, 10 μL of CCK-8 was added into each well (100 μL) and then incubated for 1 h before detection of absorbance at 450 nm by a multimode plate reader (EnVision, PerkinElmer, USA). Data were presented as means ± SD from six wells per experiment.

Cell Uptake, Lysosomal Degradation, and Intracellular Trafficking Study. PANC-1 cells (1×10^6 cells/well) were seeded in 35 mm four-well glass-bottom Petri dishes. After 24 h, the cell culture medium was replaced with DMEM (FBS-free or 10% FBS) to maintain starved or fed condition, and the cells were treated with 1 mg/mL FITC-dextran (15 kDa) with or without EIPA (25 or 50 μM). For the EIPA treatment, cells were pretreated with the predetermined concentration of EIPA for 30 min as previously reported.[48,72] After incubation for 1 h, cells were washed with cold PBS five times, fixed with 4% PFA for 15 min, stained with DAPI for 7 min, and then observed under CLSM (Nikon Ti-E, Japan). The FITC-dextran and DAPI were excited at 488 and 405 nm, respectively. For lysosomal degradation of DQ-BSA, PANC-1 cells were incubated with 0.2 mg/mL DQ-BSA Red for 1 and 6 h before visualization under CLSM. LysoTracker was added 30 min before the end of treatment to stain the lysosomes. The DQ-BSA was excited and emitted at ~590 nm and ~620 nm. The LysoTracker was excited at 638 nm, and the emission light was collected over 663−738 nm and visualized as a green color. For the intracellular trafficking study, PANC-1 cells were seeded as before. Fluorescence-labeled T-NPSM and T-UPSM at a final polymer concentration of 0.2 mg/mL were added to the cell culture medium. LysoTracker was also used. After 1 h of incubation, cells were washed and observed under CLSM using the same procedure. The excitation wavelength of 6-TMR was 543 nm, and emission spectra were collected at 580 nm.

Caspase-3 Activity Assay. The PANC-1 cells (1×10^5 cells/well) were plated in six-well plates and treated with UPSM or NPSM for 48 h under starved or fed condition. Caspase-3 activity was detected using a caspase-3 kit according to the manufacturer's instructions. Briefly, PANC-1 cells were lysed with lysis buffer (100 μL/2×10^6 cells) for 15 min on ice, followed by centrifugation at 4 °C, 20000*g* for 10 min. Caspase-3 activity in the supernatant was determined using the kit based on the catalysis of the substrate Ac-DEVD-pNA (acetyl-Asp-Glu-Val-Asp *p*-nitroanilide) to pNA (*p*-nitroaniline), which was detected by measuring the absorbance at 405 nm on a multimode plate reader (EnVision, PerkinElmer, USA).

Cell Apoptosis Assay. For the cell apoptosis assay, 2 mL of fresh medium with 1×10^5 PANC-1 cells was added to each well of a six-well plate and allowed to attach for 24 h. After incubation with various concentrations of T-NPSM or T-UPSM for 48 h, cells were harvested by mild trypsinization. The harvested cells were washed with cold PBS and resuspended in 1× binding buffer at a density of 1×10^6 cells/mL, and 200 μL of cell suspension was mixed with 5 μL of annexin V-FITC and 10 μL of PI according to the manufacturer's protocol. After a 10 min incubation at room temperature, the cells were analyzed by flow cytometry (FACSCalibur, BD, USA). A total of 10 000 events were recorded for each analysis using FlowJo software.[73]

Metabolite Profiling of Lysosomal Amino Acids. LC/MS was used to profile and quantify the concentration of lysosomal amino acids in lysosomal extraction solutions after isolation of lysosomes. PANC-1 cells (~2.5×10^7 cells in 15 cm plates) were treated with indicated formulations, rinsed twice with cold PBS, trypsinized, and centrifuged at 500*g* for 5 min. Lysosomes were isolated by a lysosome isolation kit according to the manufacturer's instructions. Briefly, the cells were resuspended in cold PBS, counted, and centrifuged at 500*g* for 5 min again to remove supernatant before adding 400 μL of extraction reagent A, vortexing, and placing the tubes on ice for 10 min. Cell samples were transferred to a Dounce tissue grinder and homogenized for 30−40 strokes to achieve 80% breakage. The homogenate was transferred to a cold tube and centrifuged at 4 °C, 1500*g* for 10 min. The supernatant was collected and centrifuged at 4 °C, 5000*g* for 10 min again to remove cells, nuclei, and cell debris. This supernatant was further transferred to a Pro-cold ultracentrifuge tube and centrifuged at 4 °C, 30000*g* by an ultracentrifuge (Optima MAX-XP, Beckman Coulter, USA) for 20 min, discarding the supernatant and adding 400 μL of extraction reagent B. Crude lysosomes were obtained after centrifugation at 4 °C, 30000*g* for 20 min again and discarding the supernatant. A 300 μL amount of fresh extraction buffer (methanol/water = 80:20) was added to each lysosome sample and placed on ice for 5 min before centrifugation at 4 °C, 15000*g* for 10 min. The lysosomal extraction solutions were collected and evaporated under nitrogen prior to LC/MS analysis by an AB SCIEX Triple Quad 6500 mass spectrometer (AB SCIEX, Ontario, Canada) interfaced with a Shimadzu LC-30A ultra-performance liquid chromatography system (Kyoto, Japan). The standard amino acids were used to validate eluted substances and generate calibration curves. Concentration of lysosomal amino acid was calculated by taking into consideration the total cell numbers.

Toxicity Assay. Male BALB/C mice (20 ± 2 g, 6 weeks of age) were employed for the MTD study, and body weights were recorded. Briefly, mice (n = 5) were administered gradient doses of TP, T-

DOI: 10.1021/acsnano.8b08246
ACS Nano 2019, 13, 4049−4063

NPSM, UPSM, and T-UPSM *via* tail vein injection every other day for a total of four doses. The MTD of different formulations was defined as the dose when >50% died due to treatment or average body weight decreased greater than 20% of initial weight.

***In Vivo* Antitumor Efficacy.** The antitumor efficacy was evaluated in both subcutaneous and orthotopic PDAC models. Male BALB/C nude mice (20 ± 2 g, 6 weeks of age) were ordered from Beijing Vital River Laboratory Animal Technology Co., Ltd. (Beijing, China) and employed to establish subcutaneous and orthotopic xenograft models. All micelle formulations were administrated by tail vein injection every 3 days for a total of four injections (three doses of GEM every 3 days).

For the subcutaneous model, 0.1 mL of PANC-1 cells (5×10^6 cells) was injected subcutaneously in the right rear flank area of nude mice for 1−2 weeks to form xenograft tumors of approximately 100 mm^3. The subcutaneous tumor volumes were calculated using the following formula: Volume = $0.5 \times L \times W^2$, where L and W are the length and width of the tumor, respectively.

For the orthotopic model, 0.04 mL of MIA PaCa-2-luc cells (2×10^6 cells) was injected into the head of the pancreas after nude mice were anaesthetized and operated on to expose the pancreas. After establishment of the orthotopic mouse models, the mice for bioluminescence were randomly selected, recorded, and photographed at day 19 and day 47. The *in vivo* whole-body bioluminescence images were taken by a Caliper IVIS Lumina II (Caliper Life Sciences); the images were taken 10 min after intraperitoneal injection of 150 mg/kg of D-luciferin. In addition, a small fraction of the orthotopic xenograft mice were randomly selected and sacrificed at day 47, and the tumor pictures and metastasis in livers of orthotopic models were recorded. The rest of the mice were treated by the above formulations, and their survival time was reported using the Kaplan−Meier method. All animal experiments and protocols were approved by the Institutional Animal Care and Use Committee (IACUC) of Tsinghua University and carried out in accordance with the People's Republic of China Legislation Regarding the Use and Care of Laboratory Animals.

Histological Analysis. For histological analysis, tumor-bearing mice were sacrificed at the end of the experiment, and tumors or livers were collected and fixed in 10% neutral buffered formalin and embedded in paraffin blocks to prepare tissue sections. The sections were stained with hematoxylin and eosin (H&E), Ki67, and terminal deoxynucleotidyltransferase-mediated UTP end labeling (TUNEL) using standard protocols. The bright field images and fluorescence images were acquired using an optical microscope (Zeiss Axio Imager.A2m, Germany) and a fluorescence microscope (Zeiss Axio Scan. Z1, Germany), respectively.

ASSOCIATED CONTENT

Supporting Information

The Supporting Information is available free of charge on the ACS Publications website at DOI: 10.1021/acsnano.8b08246.

Synthesis and characterization of TP-nsa; degradation profile of TP-nsa; viability of MIA PaCa-2 cells after treatment of TP-nsa; CMC values of T-NPSM and T-UPSM; pH buffering effect and pH-responsive behavior in biological solutions; lysosomal degradation of DQ-BSA and metabolite profiling of lysosomal amino acids after treatment for 6 h; representative pictures of tumor metastasis to liver; representative flow cytometry figures of apoptosis of PANC-1 cells; the maximum tolerated dose of different formulations in BALB/C mice (PDF)

AUTHOR INFORMATION

Corresponding Authors

*E-mail: Jinming.Gao@UTSouthwestern.edu (J.G.).
*E-mail: qianfeng@tsinghua.edu.cn (F.Q.).

ORCID

Jinming Gao: 0000-0003-0726-5098
Feng Qian: 0000-0001-7415-6997

Author Contributions

F.Q. and J.G. came up with the initial idea of combining lysosomal pH buffering with drug delivery for cancer treatment. C.K. and F.Q. designed the experiments. C.K. performed the experiments. Y.L. synthesized the pH-sensitive copolymers. Y.L., Z.L., J.Y., Z.W., L.Z., H.L., C.L., and H.P. assisted in the experiments. C.K. and F.Q. analyzed and interpreted the data. C.K. and F.Q. wrote the manuscript, and J.G. helped with revision.

Notes

The authors declare no competing financial interest.

ACKNOWLEDGMENTS

This research is supported by Beijing Advanced Innovation Center for Structural Biology, China National Nature Science Foundation (project number 81773649), and Novagenesis Theraputix (Hong Kong) Limited. F.Q. also thanks the start-up fund provided by the Center for Life Sciences at Tsinghua and Peking Universities (Beijing, China). J.G. acknowledges the support from the National Institutes of Health (R01CA192221 and R01CA211930).

REFERENCES

(1) Steward, B.; Wild, C.; Stewart, B.; Wild, C. World Cancer Report 2014 International Agency for Research on Cancer*World Health Organization*; International Agency for Research on Cancer, World Health Organization 2014.

(2) Ying, H.; Dey, P.; Yao, W.; Kimmelman, A. C.; Draetta, G. F.; Maitra, A.; DePinho, R. A. Genetics and Biology of Pancreatic Ductal Adenocarcinoma. *Genes Dev.* **2016**, *30*, 355−385.

(3) Ryan, D. P.; Hong, T. S.; Bardeesy, N. Pancreatic Adenocarcinoma. *N. Engl. J. Med.* **2014**, *371*, 1039−1049.

(4) Biankin, A. V.; Waddell, N.; Kassahn, K. S.; Gingras, M.-C.; Muthuswamy, L. B.; Johns, A. L.; Miller, D. K.; Wilson, P. J.; Patch, A.-M.; Wu, J. Pancreatic Cancer Genomes Reveal Aberrations in Axon Guidance Pathway Genes. *Nature* **2012**, *491*, 399−405.

(5) Papke, B.; Der, C. J. Drugging Ras: Know the Enemy. *Science* **2017**, *355*, 1158−1163.

(6) Bryant, K. L.; Mancias, J. D.; Kimmelman, A. C.; Der, C. J. Kras: Feeding Pancreatic Cancer Proliferation. *Trends Biochem. Sci.* **2014**, *39*, 91−100.

(7) Mccormick, F. K-Ras Protein as a Drug Target. *J. Mol. Med.* **2016**, *94*, 253−258.

(8) Heinemann, V.; Reni, M.; Ychou, M.; Richel, D.; Macarulla, T.; Ducreux, M. Tumour−Stroma Interactions in Pancreatic Ductal Adenocarcinoma: Rationale and Current Evidence for New Therapeutic Strategies. *Cancer Treat. Rev.* **2014**, *40*, 118−128.

(9) Neoptolemos, J. P.; Kleeff, J.; Michl, P.; Costello, E.; Greenhalf, W.; Palmer, D. H. Therapeutic Developments in Pancreatic Cancer: Current and Future Perspectives. *Nat. Rev. Gastroenterol. Hepatol.* **2018**, *15*, 333−348.

(10) Rd, J. B.; Yarchoan, M.; Lee, V.; Laheru, D. A.; Jaffee, E. M. Strategies for Increasing Pancreatic Tumor Immunogenicity. *Clin. Cancer Res.* **2017**, *23*, 1656−1669.

(11) Silvestris, N.; Gnoni, A.; Elisabetta Brunetti, A.; Vincenti, L.; Santini, D.; Tonini, G.; Merchionne, F.; Maiello, E.; Lorusso, V.; Nardulli, P. Target Therapies in Pancreatic Carcinoma. *Curr. Med. Chem.* **2014**, *21*, 948−965.

(12) Semaan, A.; Maitra, A. Pancreatic Cancer in 2017: Rebooting Pancreatic Cancer Knowledge and Treatment Options. *Nat. Rev. Gastroenterol. Hepatol.* **2018**, *15*, 76−78.

(13) Kamphorst, J. J.; Nofal, M.; Commisso, C.; Hackett, S. R.; Lu, W.; Grabocka, E.; Vander Heiden, M. G.; Miller, G.; Drebin, J. A.;

DOI: 10.1021/acsnano.8b08246
ACS Nano 2019, 13, 4049−4063

Bar-Sagi, D. Human Pancreatic Cancer Tumors Are Nutrient Poor and Tumor Cells Actively Scavenge Extracellular Protein. *Cancer Res.* **2015**, *75*, 544−553.
(14) Wilhelm; Park, Y.; Wright, K.; Pavlova, N.; nbsp; Tuveson, The Utilization of Extracellular Proteins as Nutrients Is Suppressed by Mtorc1. *Cell* **2015**, *162*, 259−270.
(15) Commisso, C.; Davidson, S. M.; Soydaner-Azeloglu, R. G.; Parker, S. J.; Kamphorst, J. J.; Hackett, S.; Grabocka, E.; Nofal, M.; Drebin, J. A.; Thompson, C. B. Macropinocytosis of Protein Is an Amino Acid Supply Route in Ras-Transformed Cells. *Nature* **2013**, *497*, 633−637.
(16) Perera, R. M.; Stoykova, S.; Nicolay, B. N.; Ross, K. N.; Fitamant, J.; Boukhali, M.; Lengrand, J.; Deshpande, V.; Selig, M. K.; Ferrone, C. R. Transcriptional Control of Autophagy-Lysosome Function Drives Pancreatic Cancer Metabolism. *Nature* **2015**, *524*, 361−365.
(17) Recouvreux, M. V.; Commisso, C. Macropinocytosis: A Metabolic Adaptation to Nutrient Stress in Cancer. *Front. Endocrinol. (Lausanne, Switz.)* **2017**, *8*, 261.
(18) Kimmelman, A. C. Metabolic Dependencies in Ras-Driven Cancers. *Clin. Cancer Res.* **2015**, *21*, 1828−1834.
(19) Pavlova, N. N.; Thompson, C. B. The Emerging Hallmarks of Cancer Metabolism. *Cell Metab.* **2016**, *23*, 27−47.
(20) Vander Heiden, M. G.; DeBerardinis, R. J. Understanding the Intersections between Metabolism and Cancer Biology. *Cell* **2017**, *168*, 657−669.
(21) Perera, R. M.; Zoncu, R. The Lysosome as a Regulatory Hub. *Annu. Rev. Cell Dev. Biol.* **2016**, *32*, 223−253.
(22) Settembre, C.; Fraldi, A.; Medina, D. L.; Ballabio, A. Signals from the Lysosome: A Control Centre for Cellular Clearance and Energy Metabolism. *Nat. Rev. Mol. Cell Biol.* **2013**, *14*, 283−96.
(23) Maxfield, F. R.; Willard, J. M.; Lu, S. *Lysosomes: Biology, Diseases, and Therapeutics*; John Wiley & Sons, 2016.
(24) Wang, Y.; Wang, C.; Yang, L.; Gang, H.; Tian, Z.; Ma, X.; Wang, Z.; Sumer, B. D.; White, M. A.; Gao, J. Digitization of Endocytic Ph by Hybrid Ultra-Ph-Sensitive Nanoprobes at Single-Organelle Resolution. *Adv. Mater.* **2017**, *29*, 1603794.
(25) Rabinowitz, J. D.; White, E. Autophagy and Metabolism. *Science* **2010**, *330*, 1344−8.
(26) Kroemer, G.; Jäättelä, M. Lysosomes and Autophagy in Cell Death Control. *Nat. Rev. Cancer* **2005**, *5*, 886−897.
(27) Abu-Remaileh, M.; Wyant, G. A.; Kim, C.; Laqtom, N. N.; Abbasi, M.; Chan, S. H.; Freinkman, E.; Sabatini, D. M. Lysosomal Metabolomics Reveals V-Atpase and Mtor-Dependent Regulation of Amino Acid Efflux from Lysosomes. *Science* **2017**, *358*, 807−813.
(28) Perera, R. M.; Bardeesy, N. Pancreatic Cancer Metabolism - Breaking It Down to Build It Back Up. *Cancer Discovery* **2015**, *5*, 1247−1261.
(29) Altman, B. J.; Stine, Z. E.; Dang, C. V. From Krebs to Clinic: Glutamine Metabolism to Cancer Therapy. *Nat. Rev. Cancer* **2016**, *16*, 619−634.
(30) Appelqvist, H.; Wäster, P.; Kågedal, K.; Öllinger, K. The Lysosome: From Waste Bag to Potential Therapeutic Target. *J. Mol. Cell Biol.* **2013**, *5*, 214−226.
(31) Wang, C.; Wang, Y.; Li, Y.; Bodemann, B.; Zhao, T.; Ma, X.; Huang, G.; Hu, Z.; Deberardinis, R. J.; White, M. A. A Nanobuffer Reporter Library for Fine-Scale Imaging and Perturbation of Endocytic Organelles. *Nat. Commun.* **2015**, *6*, 862−872.
(32) Nylandsted, J.; Gyrd-Hansen, M.; Danielewicz, A.; Fehrenbacher, N.; Lademann, U.; Høyer-Hansen, M.; Weber, E.; Multhoff, G.; Rohde, M.; Jäättelä, M. Heat Shock Protein 70 Promotes Cell Survival by Inhibiting Lysosomal Membrane Permeabilization. *J. Exp. Med.* **2004**, *200*, 425−435.
(33) Titov, D. V.; Gilman, B.; He, Q. L.; Bhat, S.; Low, W. K.; Dang, Y.; Smeaton, M.; Demain, A. J.; Miller, P. S.; Kugel, J. F. Xpb, a Subunit of Tfiih, Is a Target of the Natural Product Triptolide. *Nat. Chem. Biol.* **2011**, *7*, 182−188.
(34) Li, Y.; Zhao, T.; Wang, C.; Lin, Z.; Huang, G.; Sumer, B. D.; Gao, J. Molecular Basis of Cooperativity in Ph-Triggered Supramolecular Self-Assembly. *Nat. Commun.* **2016**, *7*, 13214.
(35) He, Q. L.; Minn, I.; Wang, Q.; Xu, P.; Head, S. A.; Datan, E.; Yu, B.; Pomper, M. G.; Liu, J. O. Targeted Delivery and Sustained Antitumor Activity of Triptolide through Glucose Conjugation. *Angew. Chem.* **2016**, *55*, 12214−12218.
(36) Kataoka, K.; Harada, A.; Nagasaki, Y. Block Copolymer Micelles for Drug Delivery: Design, Characterization and Biological Significance. *Adv. Drug Delivery Rev.* **2012**, *64*, 37−48.
(37) Rösler, A.; Vandermeulen, G. W.; Klok, H.-A. Advanced Drug Delivery Devices *Via* Self-Assembly of Amphiphilic Block Copolymers. *Adv. Drug Delivery Rev.* **2012**, *64*, 270−279.
(38) Zhang, L.; Chen, Z.; Yang, K.; Liu, C.; Gao, J.; Qian, F. B-Lapachone and Paclitaxel Combination Micelles with Improved Drug Encapsulation and Therapeutic Synergy as Novel Nanotherapeutics for Nqo1-Targeted Cancer Therapy. *Mol. Pharmaceutics* **2015**, *12*, 3999−4010.
(39) Zhu, M.; Nie, G.; Meng, H.; Xia, T.; Nel, A.; Zhao, Y. Physicochemical Properties Determine Nanomaterial Cellular Uptake, Transport, and Fate. *Acc. Chem. Res.* **2013**, *46*, 622−631.
(40) Duan, X.; Li, Y. Physicochemical Characteristics of Nanoparticles Affect Circulation, Biodistribution, Cellular Internalization, and Trafficking. *Small* **2013**, *9*, 1521−1532.
(41) He, C.; Hu, Y.; Yin, L.; Tang, C.; Yin, C. Effects of Particle Size and Surface Charge on Cellular Uptake and Biodistribution of Polymeric Nanoparticles. *Biomaterials* **2010**, *31*, 3657−66.
(42) Zhou, K.; Wang, Y.; Huang, X.; Luby-Phelps, K.; Sumer, B. D.; Gao, J. Tunable, Ultrasensitive Ph-Responsive Nanoparticles Targeting Specific Endocytic Organelles in Living Cells. *Angew. Chem., Int. Ed.* **2011**, *50*, 6109−6114.
(43) Li, Y.; Wang, Z.; Wei, Q.; Luo, M.; Huang, G.; Sumer, B. D.; Gao, J. Non-Covalent Interactions in Controlling Ph-Responsive Behaviors of Self-Assembled Nanosystems. *Polym. Chem.* **2016**, *7*, 5949−5956.
(44) Kang, M.; Lam, D.; Discher, D. E.; Loverde, S. M. *Molecular Modeling of Block Copolymer Self-Assembly and Micellar Drug Delivery*; Wiley-Blackwell, 2015.
(45) Casey, J. R.; Grinstein, S.; Orlowski, J. Sensors and Regulators of Intracellular Ph. *Nat. Rev. Mol. Cell Biol.* **2010**, *11*, 50−61.
(46) Mindell, J. A. Lysosomal Acidification Mechanisms. *Annu. Rev. Physiol.* **2012**, *74*, 69−86.
(47) Pisco, A. O.; Jackson, D. A.; Huang, S. Reduced Intracellular Drug Accumulation in Drug-Resistant Leukemia Cells Is Not Only Solely Due to Mdr-Mediated Efflux but Also to Decreased Uptake. *Front. Oncol.* **2014**, *4*, 306.
(48) Cosimo, C.; Rory, J. F.; Dafna, B.-S. Determining the Macropinocytic Index of Cells through a Quantitative Image-Based Assay. *Nat. Protoc.* **2014**, *9*, 182−192.
(49) Reis, R. C. M.; Sorgine, M. H. F.; Coelho-Sampaio, T. A Novel Methodology for the Investigation of Intracellular Proteolytic Processing in Intact Cells. *Eur. J. Cell Biol.* **1998**, *75*, 192−197.
(50) Hanahan, D.; Weinberg, R. A. Hallmarks of Cancer: The Next Generation. *Cell* **2011**, *144*, 646−674.
(51) Poon, I. K.; Lucas, C. D.; Rossi, A. G.; Ravichandran, K. S. Apoptotic Cell Clearance: Basic Biology and Therapeutic Potential. *Nat. Rev. Immunol.* **2014**, *14*, 166−180.
(52) Kerr, J. F. R.; Wyllie, A. H.; Currie, A. R. Apoptosis: A Basic Biological Phenomenon with Wideranging Implications in Tissue Kinetics. *Br. J. Cancer* **1972**, *26*, 239−257.
(53) Son, J.; Lyssiotis, C. A.; Ying, H.; Wang, X.; Hua, S.; Ligorio, M.; Perera, R. M.; Ferrone, C. R.; Mullarky, E.; Shyhchang, N. Glutamine Supports Pancreatic Cancer Growth through a Kras-Regulated Metabolic Pathway. *Nature* **2013**, *496*, 101−105.
(54) Olivares, O.; Mayers, J. R.; Gouirand, V.; Torrence, M. E.; Gicquel, T.; Borge, L.; Lac, S.; Roques, J.; Lavaut, M. N.; Berthezène, P. Collagen-Derived Proline Promotes Pancreatic Ductal Adenocarcinoma Cell Survival under Nutrient Limited Conditions. *Nat. Commun.* **2017**, *8*, 16031.

DOI: 10.1021/acsnano.8b08246
ACS Nano 2019, 13, 4049−4063

(55) Olivares, O.; Vasseur, S. Metabolic Rewiring of Pancreatic Ductal Adenocarcinoma: New Routes to Follow within the Maze. *Int. J. Cancer* **2016**, *138*, 787−796.
(56) Yu, H.; Zou, Y.; Wang, Y.; Huang, X.; Huang, G.; Sumer, B. D.; Boothman, D. A.; Gao, J. Overcoming Endosomal Barrier by Amphotericin B-Loaded Dual Ph-Responsive Pdma- B -Pdpa Micelleplexes for Sirna Delivery. *ACS Nano* **2011**, *5*, 9246−55.
(57) Zhu, W.; Li, J.; Wu, S.; Li, S.; Le, L.; Su, X.; Qiu, P.; Hu, H.; Yan, G. Triptolide Cooperates with Cisplatin to Induce Apoptosis in Gemcitabine-Resistant Pancreatic Cancer. *Pancreas* **2012**, *41*, 1029−1038.
(58) Li, C.-J.; Chu, C.-Y.; Huang, L.-H.; Wang, M.-H.; Sheu, L.-F.; Yeh, J.-I.; Hsu, H.-Y. Synergistic Anticancer Activity of Triptolide Combined with Cisplatin Enhances Apoptosis in Gastric Cancer *in Vitro* and *in Vivo*. *Cancer Lett.* **2012**, *319*, 203−213.
(59) Lei, Y.; Tang, T.; Xie, X.; Xianyu, X.; Zhang, Z.; Wang, W.; Hamada, H.; Jiang, J.; Zheng, Z.; Jiang, J. Gold Nanoclusters-Assisted Delivery of Ngf Sirna for Effective Treatment of Pancreatic Cancer. *Nat. Commun.* **2017**, *8*, 15130.
(60) Hoffman, R. M. Patient-Derived Orthotopic Xenografts: Better Mimic of Metastasis Than Subcutaneous Xenografts. *Nat. Rev. Cancer* **2015**, *15*, 451−452.
(61) Chugh, R.; Sangwan, V.; Patil, S. P.; Dudeja, V.; Dawra, R. K.; Banerjee, S.; Schumacher, R. J.; Blazar, B. R.; Georg, G. I.; Vickers, S. M. A Preclinical Evaluation of Minnelide as a Therapeutic Agent against Pancreatic Cancer. *Sci. Transl. Med.* **2012**, *4* (156), 156ra139.
(62) Cox, A. D.; Fesik, S. W.; Kimmelman, A. C.; Luo, J.; Der, C. J. Drugging the Undruggable Ras: Mission Possible? *Nat. Rev. Drug Discovery* **2014**, *13*, 828−851.
(63) Ganta, S.; Devalapally, H.; Shahiwala, A.; Amiji, M. A Review of Stimuli-Responsive Nanocarriers for Drug and Gene Delivery. *J. Controlled Release* **2008**, *126*, 187−204.
(64) Liu, J.; Huang, Y.; Kumar, A.; Tan, A.; Jin, S.; Mozhi, A.; Liang, X.-J. Ph-Sensitive Nano-Systems for Drug Delivery in Cancer Therapy. *Biotechnol. Adv.* **2014**, *32*, 693−710.
(65) Kanamala, M.; Wilson, W. R.; Yang, M.; Palmer, B. D.; Wu, Z. Mechanisms and Biomaterials in Ph-Responsive Tumour Targeted Drug Delivery: A Review. *Biomaterials* **2016**, *85*, 152−167.
(66) Hingorani, S. R.; Wang, L.; Multani, A. S.; Combs, C.; Deramaudt, T. B.; Hruban, R. H.; Rustgi, A. K.; Chang, S.; Tuveson, D. A. Trp53r172h and Krasg12d Cooperate to Promote Chromosomal Instability and Widely Metastatic Pancreatic Ductal Adenocarcinoma in Mice. *Cancer Cell* **2005**, *7*, 469−483.
(67) Gopinathan, A.; Morton, J. P.; Jodrell, D. I.; Sansom, O. J. Gemms as Preclinical Models for Testing Pancreatic Cancer Therapies. *Dis. Models & Mech.* **2015**, *8*, 1185−1200.
(68) Dunne, R. F.; Hezel, A. F. Genetics and Biology of Pancreatic Ductal Adenocarcinoma. *Hematol. Oncol. Clin. North Am.* **2015**, *20*, 595−608.
(69) Shim, W. S.; Lee, J. S.; Lee, D. S. Ph-Induced Micellization of Biodegradable Block Copolymers Containing Sulfamethazine. *Macromol. Res.* **2005**, *13*, 344−351.
(70) Aguiar, J.; Carpena, P.; Molina-BolíVar, J. A.; Ruiz, C. C. On the Determination of the Critical Micelle Concentration by the Pyrene 1:3 Ratio Method. *J. Colloid Interface Sci.* **2003**, *258*, 116−122.
(71) Fontana, G.; Licciardi, M.; Mansueto, S.; Schillaci, D.; Giammona, G. Amoxicillin-Loaded Polyethylcyanoacrylate Nanoparticles: Influence of Peg Coating on the Particle Size, Drug Release Rate and Phagocytic Uptake. *Biomaterials* **2001**, *22*, 2857−2865.
(72) Cullis, J.; Siolas, D.; Avanzi, A.; Barui, S.; Maitra, A.; Bar-Sagi, D. Macropinocytosis of Nab-Paclitaxel Drives Macrophage Activation in Pancreatic Cancer. *Cancer Immunol. Res.* **2017**, *5*, 182−190.
(73) Lai, X.; Broderick, R.; Bergoglio, V.; Zimmer, J.; Badie, S.; Niedzwiedz, W.; Hoffmann, J.-S.; Tarsounas, M. Mus81 Nuclease Activity Is Essential for Replication Stress Tolerance and Chromosome Segregation in Brca2-Deficient Cells. *Nat. Commun.* **2017**, *8*, 15983.

DOI: 10.1021/acsnano.8b08246
ACS Nano 2019, 13, 4049−4063